The Optical Properties of Nitride Semiconductors for Visible Light Emission

by

Ti Li

A Dissertation Presented in Partial Fulfillment
of the Requirements for the Degree
Doctor of Philosophy

Approved November 2012 by the
Graduate Supervisory Committee:

Fernando A. Ponce, Chair
Robert Culbertson
Hongbin Yu
John Shumway
José Menéndez

ARIZONA STATE UNIVERSITY

December 2012

ABSTRACT

Nitride semiconductors have wide applications in electronics and optoelectronics technologies. Understanding the nature of the optical recombination process and its effects on luminescence efficiency is important for the development of novel devices. This dissertation deals with the optical properties of nitride semiconductors, including GaN epitaxial layers and more complex heterostructures. The emission characteristics are examined by cathodoluminescence spectroscopy and imaging, and are correlated with the structural and electrical properties studied by transmission electron microscopy and electron holography. Four major areas are covered in this dissertation, which are described next.

The effect of strain on the emission characteristics in wurtzite GaN has been studied. The values of the residual strain in GaN epilayers with different dislocation densities are determined by x-ray diffraction, and the relationship between exciton emission energy and the in-plane residual strain is demonstrated. It shows that the emission energy increases withthe magnitude of the in-plane compressive strain.

The temperature dependence of the emission characteristics in cubic GaN has been studied. It is observed that the exciton emission and donor-acceptor pair recombination behave differently with temperature. The donor-bound exciton binding energy has been measured to be 13 meV from the temperature dependence of the emission spectrum. It is also found that the ionization energies for both acceptors and donors are smaller in cubic compared with hexagonal structures, which should contribute to higher doping efficiencies.

A comprehensive study on the structural and optical properties is presented for InGaN/GaN quantum wells emitting in the blue, green, and yellow regions of the electromagnetic spectrum. Transmission electron microscopy images indicate the

presence of indium inhomogeneties which should be responsible for carrier localization. The temperature dependence of emission luminescence shows that the carrier localization effects become more significant with increasing emission wavelength. On the other hand, the effect of non-radiative recombination on luminescence efficiency also varies with the emission wavelength. The fast increase of the non-radiative recombination rate with temperature in the green emitting QWs contributes to the lower efficiency compared with the blue emitting QWs. The possible saturation of non-radiative recombination above 100 K may explain the unexpected high emission efficiency for the yellow emitting QWs

Finally, the effects of InGaN underlayers on the electronic and optical properties of InGaN/GaN quantum wells emitting in visible spectral regions have been studied. A significant improvement of the emission efficiency is observed, which is associated with a blue shift in the emission energy, a reduced recombination lifetime, an increased spatial homogeneity in the luminescence, and a weaker internal field across the quantum wells. These are explained by a partial strain relaxation introduced by the InGaN underlayer, which is measured by reciprocal space mapping of the x-ray diffraction intensity.

DEDICATION

To my parents and my husband.

ACKNOWLEDGMENTS

It was a big challenge for me when I started my study and research at ASU. At that time, I had been away from school for two years, after getting my master's degree from Peking University in China. I was not confident about my language and research skills. It is very fortunate for me that I got help from Prof. Fernando Ponce. He taught me a lot about how to approach research problems, how to analyze and understand the results from a physicist's perspective. Thanks to him, I developed my own way of critical and independent thinking in research. His patience and support have meant a lot to me.

I would also like to thank my husband, Qiyuan Wei, who is also a former member in our research group. He encouraged me to come to ASU, and we have worked together for four years, and have learnt from each other in many ways.

I am also extremely grateful to Dr. Alec Fischer. He taught me so many things, how to do cathodoluminescence spectroscopy and imaging, and how to analyze experimental data. It has been a wonderful experience to work with him.

I am grateful to Dr. Zhihao Wu, Dr. Yu Huang, Dr. Kewei Sun, Mr. Reid Juday, Ms. Jingyi Huang and Mr. Yong Wei for their collaboration.

I am also grateful to my PhD Committee members: Prof. Robert Culbertson, Prof. John Shumway, Prof. Jose Menendez, and Prof. Hongbin Yu, for their advice and help with this dissertation.

TABLE OF CONTENTS

Page

LIST OF TABLES

Table Page

LIST OF FIGURES

Figure Page

Figure Page

CHAPTER 1

INTRODUCTION TO LIGHT EMISSION IN SEMICONDUCTORS

1.1 PHOTON GENERATION BY LIGHT EMITTING DIODES

Generation of light by *p*-*n* junction diodes made of compound semiconductors has been a great achievement in human history. It represents an improvement over older technologies by directly and efficiently converting electric energy to light. This successful application has made light emission in semiconductors an active and interesting research topic.

Figure 1.1 shows the principles of a *p*-*n* junction in light emitting diodes (LED). LEDs consist of a stacked sandwich of *p*-type and *n*-type materials. Plotted are the energies for conduction band (E_c), valence band (E_v) and Fermi energy (E_F). Forward bias on the junction enables electrons to diffuse from the *n*-side towards the *p*-side, encountering holes diffusing in the opposite direction. Thus, an excess of minority carriers are created within the junction region, which leads to electron and hole recombination. Such recombination can result in an emission of photons (i.e. radiative), whose energy are close to the band gap E_g.

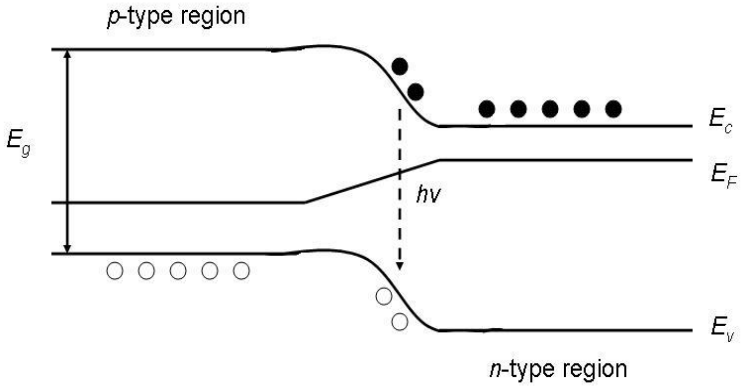

Fig. 1.1. Schematic diagram of a *p*-*n* junction showing the conduction band (E_c), the valence band (E_v), and the Fermi energy (E_F). Solid and open spheres represent electrons and holes, respectively.

Double heterostructures (DH) provide higher light emission efficiencies than homojunctions. A DH LED structure is shown in Fig. 1.2. It consists of an active region where recombination

occurs, and two confinement layers that have larger band gaps than the active region. Quantum wells (QW) are frequently used in the active region to provide additional carrier confinement.

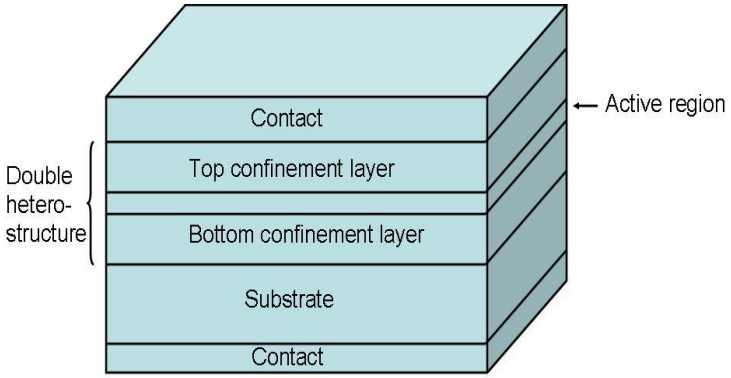

Fig. 1.2. Schematic structure of a double heterostructure LED consisting an active region and two confinement layers.

Proper choice of semiconductors in the heterostructures is required for efficient and desired light emission. Direct band gap materials with ability of both *p*- type and *n*- type doping are favored. Nitride semiconductors, for example, are successful choices for light emitting applications.

1.2 NITRIDE SEMICONDUCTORS FOR LIGHT EMITTING DIODES

There are two primary reasons for choosing nitride semiconductors for light emitting diodes. One is the strong chemical bond between Ga and N that makes the material stable under high injection current or intense light exposure. The other is that the Al-Ga-In-N system has a large direct band gap range covering the entire visible spectrum. Figure 1.3 shows the band gap energy as a function of chemical composition x for $Al_xGa_{1-x}N$ and $In_xGa_{1-x}N$ alloys. The color blocks represent the energy range of the entire visible spectrum. The band gaps of AlN, GaN, and InN at room temperature are 6.18, 3.43, and 0.70 eV, respectively. The band gap of their ternary alloys can be calculated by

$$E_g(A_xB_{1-x}N) = xE_g(AN) + (1-x)E_g(BN) - bx(1-x) \qquad (1.1)$$

where *A* and *B* denote Al, Ga, or In elements, and *b* is bowing parameter. The bowing parameters of AlGaN and InGaN used in Fig 1.3 are 0.7 eV and 1.4 eV, respectively.[1]

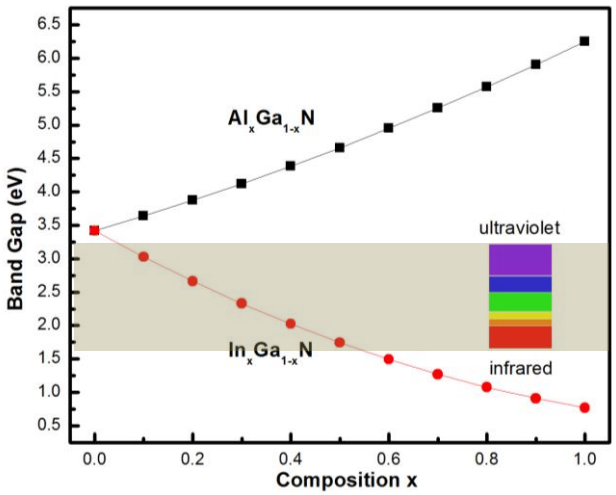

Fig. 1.3. The band gap energy as a function of chemical composition *x* for $Al_xGa_{1-x}N$ and $In_xGa_{1-x}N$ alloys, and the color blocks represent corresponding energy range in the visible spectrum. The band gap energies are calculated using Eq. (1.1) and bowing parameters 0.7 eV and 1.4 eV for AlGaN and InGaN, respectively.

P-type and *n*-type doping are also of great importance for light emitting applications. For nitride semiconductors, *p*-type doping is considered a big challenge since the very beginning of its development. Until the late 1980's, *p*-type conductive GaN was believed impossible to achieve due to self-compensation from residual donors, like nitrogen vacancies, and possible formation of Mg-H complexes.[2,3] The introduction of low-temperature buffer layer reduces the intrinsic impurities to less than $10^{17}/cm^3$, opening the possibility for efficient *p*-doping.[4,5] A breakthrough was made in 1989 when *p*-type conducting GaN was achieved using low energy electron beam irradiation on as-grown Mg-doped GaN, in which the electron beam dissociates the Mg-H complex and rendered Mg into an active dopant.[6] Later in 1991, Nakamura showed that by thermal annealing Mg-doped GaN, at temperatures up to 1000^oC and under hydrogen-free atmosphere, provides a faster and easier way for producing p-type conducting GaN.[7]

The first commercial blue LEDs made by nitride semiconductors were available in early 1994 by Nichia. From then on, devices with longer emission wavelengths have been fabricated

using InGaN-based QWs. The commonly used layer structure is demonstrated in Fig. 1.4. It consists of a *p*-*n* junction such that when a forward bias is applied, the electrons and holes are injected toward the active region and recombine with each other. The QWs are used in the active region for better carrier confinement, so that a more efficient light emission with narrower spectra width can be obtained. GaN layers with wider band gap than the InGaN wells are used as the confinement layers, commonly called waveguides.

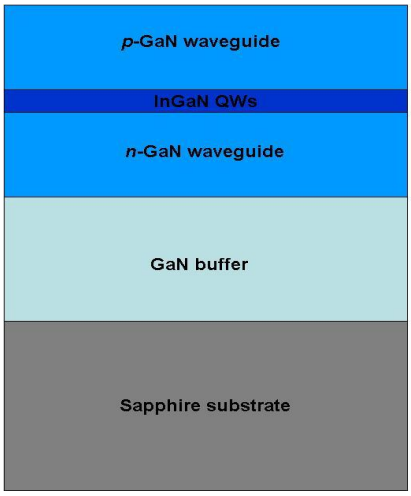

Fig. 1.4. Device structure of a light emitting diode using InGaN QWs as active region and GaN as waveguides.

My research work has focused on the optical properties of GaN-based materials and devices for light emitting application. Useful information can be found by studying optical emissions from materials and devices. Foremost is the characteristic emission peak energy (or wavelength) combined with knowledge of radiative recombination dynamics, which are associated with various recombination mechanisms. Furthermore is the response of emission characteristics to all kinds of perturbations, for example, temperature, strain, or injection current. The following sections will elaborate these emission features with details.

1.3 LIGHT EMISSION CHARACTERISTICS

Electron-hole recombination results in light emission, and this process is illustrated in Fig. 1.5. In the vicinity of band edge (k=0), the energies of electrons in the conduction band and holes

in the valence band can be expressed using parabolic approximations, in which the electrons are treated similar to free particles with plane-wave functions, and the free electron mass is replace by the effective mass to represent the influence of the crystal lattice.

$$E = E_c + \frac{\hbar^2 k^2}{2m_e^*} \quad \text{(for electrons)} \tag{1.2}$$

$$E = E_v - \frac{\hbar^2 k^2}{2m_h^*} \quad \text{(for holes)} \tag{1.3}$$

where m_e^* and m_h^* are the electron and hole effective masses; E_c and E_v are the conduction and valence band edges; k is the wave vector for the electrons and holes. The effective masses of electron and hole in GaN have been reported to be $m_e^* = 0.20\, m_0$ and $m_h^* = 1.10 m_0$.[8] For a direct electron-hole recombination in which electrons and holes have the same momentum or k value, using Eq. (1.2) and (1.3), the photon energy can be written as:

$$h\nu = E_c + \frac{\hbar^2 k^2}{2m_e^*} - (E_v - \frac{\hbar^2 k^2}{2m_h^*}) = E_g + \frac{\hbar^2 k^2}{2m_r^*} \tag{1.4}$$

in which m_r^* is the reduced mass given by $\frac{1}{m_r^*} = \frac{1}{m_e^*} + \frac{1}{m_h^*}$.

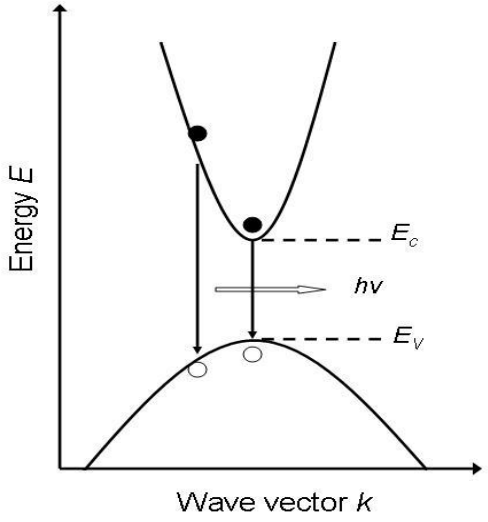

Fig. 1.5. Energy dispersion plot showing electron-hole recombination mechanisms that conserve momentum.

The emission intensity at a certain energy given by Eq. (1.4) is proportional to the carrier concentration, which is the product of the joint density of states and carrier distribution function. The joint density of states is given by

$$N(E) = \frac{1}{2\pi^2}\left(\frac{2m_r^*}{\hbar^2}\right)^{3/2}\sqrt{E - E_g} \tag{1.5}$$

The distribution of carriers is given by the Boltzmann distribution,

$$f_B(E) = e^{-E/(k_B T)} \tag{1.6}$$

So the emission intensity I as a function of emission energy E is proportional to the product of Eq. (1.5) and (1.6),

$$I(E) \propto \sqrt{E - E_g}\, e^{-E/(k_B T)} \tag{1.7}$$

Based on Eq. (1.7), the theoretical emission spectrum of an LED is shown is Fig. 1.6. The maximum intensity occurs at

$$E = E_g + \tfrac{1}{2} k_B T \tag{1.8}$$

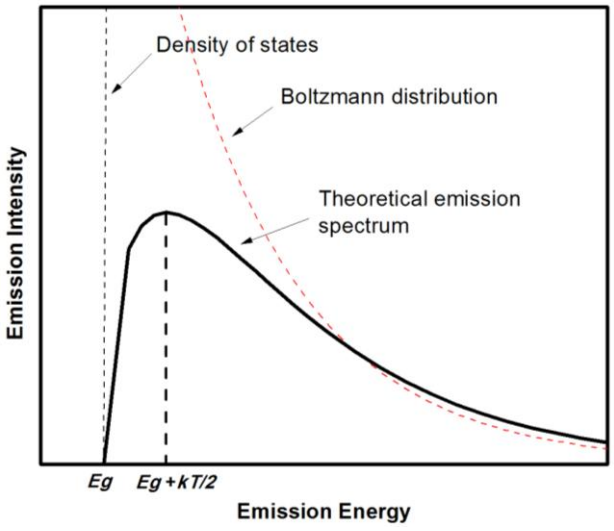

Fig. 1.6. Theoretical emission spectrum of an LED with maximum intensity at $E = E_g + \frac{1}{2} k_B T$.

1.4 RADIATIVE RECOMBINATION RATES

The derivation of the radiative recombination rate is dealt with time-dependent perturbation theory in quantum mechanics.[9] The perturbation due to electromagnetic radiation (photon) will be disucussed next.. The interaction of photons with electrons in a semiconductor material can be described by the following Hamiltonian:

$$\begin{aligned} H &= \frac{1}{2m_0}(\mathbf{p} - e\mathbf{A})^2 + V(\mathbf{r}) \\ &= \frac{\mathbf{p}^2}{2m_0} + V(\mathbf{r}) - \frac{e}{2m_0}(\mathbf{p}\cdot\mathbf{A} + \mathbf{A}\cdot\mathbf{p}) + \frac{e^2\mathbf{A}^2}{2m_0} \end{aligned} \tag{1.9}$$

where m_0 is the free electron mass, **A** is the vector potential accounting for the electromagnetic field, and $V(\mathbf{r})$ is the periodic potential in the crystal. Using Coulomb gauge $\nabla\cdot\mathbf{A} = 0$ and for most practical optical field, Eq. (1.9) can be expressed as:

$$H = H_0 + H'$$

$$H_0 = \frac{\mathbf{p}^2}{2m_0} + V(\mathbf{r}) \tag{1.10}$$

$$H' \cong -\frac{e}{m_0}\mathbf{A}\cdot\mathbf{p} \tag{1.11}$$

in which H_0 is the unperturbed Hamiltonian, and H' is the perturbation of photon.

Assuming the vector potential has the form of

$$\begin{aligned} \mathbf{A} &= \hat{e}\,A_0\cos(\mathbf{k}_{op}\cdot\mathbf{r} - \omega t) \\ &= \hat{e}\frac{A_0}{2}e^{i\mathbf{k}_{op}\cdot\mathbf{r}}e^{-i\omega t} + \hat{e}\frac{A_0}{2}e^{-i\mathbf{k}_{op}\cdot\mathbf{r}}e^{i\omega t} \end{aligned} \tag{1.12}$$

where $\hat{e}$ is the unit vector in the direction of the optical electric field, $\mathbf{k}_{op}$ is the wave vector, and ω is the angular frequency. The perturbed Hamiltonian in Eq. (1.11) can then be written as:

$$H'(\mathbf{r},t) = -\frac{e}{m_0}\mathbf{A}(\mathbf{r},t)\cdot\mathbf{p} = H'(\mathbf{r})e^{-i\omega t} + H'^{+}(\mathbf{r})e^{+i\omega t} \tag{1.13}$$

where $H'(r) = -\frac{eA_0 e^{i\mathbf{k}_{op}\cdot\mathbf{r}}}{2m_0} \hat{e}\cdot\mathbf{p}$ (1.14)

To find solutions $\psi(\mathbf{r},t)$ to the time-dependent Schrödinger equation, the wave function is expanded in terms of unperturbed solutions:

$$\psi(\mathbf{r},t) = \sum_n a_n(t)\phi_n(\mathbf{r})e^{-iE_n t/\hbar} \tag{1.15}$$

where $\phi_n(r)$ and E_n are the wave function and eigenvalue of the state *n* for the unperturbed Hamiltonian, $|a_n(t)|^2$ represents the probability that the electron is in the state *n* at time *t*. Substituting the Eq. (1.15) into the Schrödinger equation,

$$\sum_n \frac{d\, a_n(t)}{d\, t}\phi_n(\mathbf{r})e^{-iE_n t/\hbar} = -\frac{i}{\hbar}\sum_n H'(\mathbf{r},t)a_n(t)\phi_n(\mathbf{r})e^{-iE_n t/\hbar} \tag{1.16}$$

Taking the inner product with the wave function $\phi_m^*(\mathbf{r})$ and using the orthonormal condition, the following equation can be obtained:

$$\frac{d\, a_m(t)}{d\, t} = -\frac{i}{\hbar}\sum_n a_n(t)H'_{mn}(t)e^{i\omega_{mn}t} \tag{1.17}$$

where

$$\begin{aligned} H'_{mn}(t) &= \langle m|H'(\mathbf{r},t)|n\rangle = \int \phi_m^*(\mathbf{r})H'(\mathbf{r},t)\phi_n(\mathbf{r})d^3\mathbf{r} \\ &= H'_{mn}e^{-i\omega t} + H'^{+}_{mn}e^{+i\omega t} \end{aligned} \tag{1.18}$$

$$\omega_{mn} = \frac{E_m - E_n}{\hbar} \tag{1.19}$$

and the matrix element can be defined as

$$H'_{mn} = \int \phi_m^*(\mathbf{r})H'(\mathbf{r})\phi_n(\mathbf{r})d^3\mathbf{r} \tag{1.20}$$

Assuming initially the electron stays at state *i* in the absence of any perturbation, the zeroth-order solution of the Schrödinger equation can be written as

$$a_i^{(0)}(t) = 1$$
$$a_m^{(0)}(t) = 0 \qquad m \neq i \tag{1.21}$$

Then the first-order solution is obtained from

$$\begin{aligned} \frac{d}{dt} a_f^{(1)}(t) &= \frac{-i}{\hbar} H_{fi}^{'}(t) e^{i\omega_{fi}t} \\ &= \frac{-i}{\hbar} (H_{fi}^{'} e^{i(\omega_{fi}-\omega)t} + H_{fi}^{'+} e^{i(\omega_{fi}+\omega)t}) \end{aligned} \tag{1.22}$$

By integration,

$$a_f^{(1)}(t) = \frac{-i}{\hbar} (H_{fi}^{'} \frac{e^{i(\omega_{fi}-\omega)t} - 1}{\omega_{fi} - \omega} + H_{fi}^{'+} \frac{e^{i(\omega_{fi}+\omega)t} - 1}{\omega_{fi} + \omega}) \tag{1.23}$$

The probability of the electron in the final state is given by

$$\left|a_f^{(1)}(t)\right|^2 \approx \frac{2\pi t}{\hbar^2} \left|H_{fi}^{'}\right|^2 \delta(\omega_{fi} - \omega) + \frac{2\pi t}{\hbar^2} \left|H_{fi}^{'}\right|^2 \delta(\omega_{fi} + \omega) \tag{1.24}$$

if we consider the photon energy to be near resonance, either $\omega \sim \omega_{fi}$ or $\omega \sim -\omega_{fi}$.

The transition rate is

$$\begin{aligned} W_{i\to f} &= \frac{d}{dt} \left|a_f^{(1)}(t)\right|^2 \\ &= \frac{2\pi}{\hbar} \left|H_{fi}^{'}\right|^2 \delta(E_f - E_i - \hbar\omega) + \frac{2\pi}{\hbar} \left|H_{fi}^{'}\right|^2 \delta(E_f - E_i + \hbar\omega) \end{aligned} \tag{1.25}$$

The first term corresponds to the absorption of a photon, since $E_f = E_i + \hbar\omega$. And the second term corresponds to the emission of a photon, since $E_f = E_i - \hbar\omega$.

The total emission rate from initial state *b* to final state *a* ($E_b > E_a$) per unit volume in the material, considering the probability that the initial state *b* is occupied and the final state *a* is unoccupied, is

$$R_{b\to a} = \frac{2}{V} \sum_{\mathbf{k}_a} \sum_{\mathbf{k}_b} \frac{2\pi}{\hbar} \left|H_{ba}^{'}\right|^2 \delta(E_a - E_b + \hbar\omega) f_b (1 - f_a) \tag{1.26}$$

The above equation sums over all possible initial and final states, and the prefactor 2 takes into account the sum over spins. The Fermi-Dirac distribution is assumed that

$f_a = \frac{1}{1+e^{(E_a - E_F)/k_B T}}$ is the probability that state *a* is occupied. Similarly, the total absorption rate is

$$R_{a\to b} = \frac{2}{V}\sum_{\mathbf{k}_a}\sum_{\mathbf{k}_b}\frac{2\pi}{\hbar}\left|H'_{ba}\right|^2 \delta(E_b - E_a - \hbar\omega) f_a(1-f_b) \tag{1.27}$$

So the net absorption rate per unit volume is

$$R = R_{a\to b} - R_{b\to a} = \frac{2}{V}\sum_{\mathbf{k}_a}\sum_{\mathbf{k}_b}\frac{2\pi}{\hbar}\left|H'_{ba}\right|^2 \delta(E_b - E_a - \hbar\omega)(f_a - f_b) \tag{1.28}$$

For interband transitions between the valence band and conduction band, and assuming that the valence band is completely occupied, and conduction band is empty, the net transition rate between the valence band and conduction band is

$$\begin{aligned} R = R_{v\to c} - R_{c\to v} &= \frac{2}{V}\sum_{\mathbf{k}_c}\sum_{\mathbf{k}_v}\frac{2\pi}{\hbar}\left|H'_{cv}\right|^2 \delta(E_c - E_v - \hbar\omega)(f_v - f_c) \\ &= \frac{2}{V}\sum_{\mathbf{k}_c}\sum_{\mathbf{k}_v}\frac{2\pi}{\hbar}\left|H'_{cv}\right|^2 \delta(E_c - E_v - \hbar\omega) \\ &= \frac{\pi e^2 A_0^2}{2m_0^2\hbar}\frac{2}{V}\sum_{\mathbf{k}}\left|\hat{e}\cdot\mathbf{p}_{cv}\right|^2 \delta(E_c - E_v - \hbar\omega) \end{aligned} \tag{1.29}$$

The joint density of state N_{cv} is introduced by converting the sum over *k* into the integral of energy,

$$R = \frac{\pi e^2 A_0^2}{2m_0^2\hbar}\int_0^\infty d\varepsilon_k N_{cv}(\varepsilon)\left|\hat{e}\cdot\mathbf{p}_{cv}\right|^2 \delta(E_g + \varepsilon_k - \hbar\omega) \tag{1.30}$$

The integral can be carried out analytically and obtain:

$$R = \frac{\pi e^2 A_0^2}{2m_0^2\hbar} N_{cv}(\hbar\omega - E_g)\left|\hat{e}\cdot\mathbf{p}_{cv}\right|^2 \tag{1.31}$$

The momentum matrix element can also be replaced by the electric dipole moment. Since $\mathbf{p} = m_0 \frac{d}{dt}\mathbf{r} = \frac{m_0}{i\hbar}(\mathbf{r}H_0 - H_0\mathbf{r})$,

$$\begin{aligned} \hat{e}\cdot\mathbf{p}_{cv} &= \frac{m_0}{i\hbar}\langle\phi_c|\hat{e}\cdot(\mathbf{r}H_0 - H_0\mathbf{r})|\phi_v\rangle \\ &= \frac{m_0}{i\hbar}(E_v - E_c)\langle\phi_c|\hat{e}\cdot\mathbf{r}|\phi_v\rangle \\ &= -\frac{m_0\omega}{i}\hat{e}\cdot\mathbf{r}_{cv} \end{aligned} \qquad (1.32)$$

Therefore, the net transition rate depends on the momentum-matrix element in Eq. (1.32) and the joint density of states in Eq. (1.5). The Eq. (1.32) can also be interpreted as the overlap of electron and hole wave functions. Thus, if the overlap between electron and hole wave functions is enhanced, the radiative recombination rate is increased. This effect is more pronounced in QW structures.

1.5 TEMPERATURE INDUCED EMISSION ENERGY SHIFT

The variation of energy gap with temperature is due to thermal expansion of lattice. The relation between temperature and band gap E_g in semiconductors is illustrated as Varshini's formula:[10]

$$E_g = E_0 - \alpha T^2/(T+\beta) \qquad (1.33)$$

where E_0 is the energy gap at 0 K, and α and β are constants.

Varshini's equation has successfully represented the experimental measurements for diamond, Si, Ge, 6H-SiC, GaAs, InP, and InAs.[10] For wurzite GaN, it has been reported that the fitting parameters are $\alpha = 0.375meV$ and $\beta = 270K$ for the temperature variation of free exciton A emission.[11] However, *S*-shaped temperature dependence of emission energy has been reported both in InGaN and AlGaN systems.[12-15] The experiments showed a continuous blue shift of the spectral peak position with respect to the values predicted by the Varshini's equation. This behavior can be explained by the involvement of localized states in the radiative recombination.

Eliseev et al. proposed a band-filling model involving with band-tail states, in which fluctuations in alloy composition provides the source for tail states.[16] The composition fluctuations result in local potential minimal and cause localized states in the band tails. In his model, the density of localized states is a Gaussian function having dispersions of σ^2,

$$\rho_{e,h}(E) = \rho_{0e,h} \exp[-(E - E_{0e,h})^2 / 2\sigma_{0e,h}^2] \tag{1.34}$$

where ρ_{0e}, ρ_{0h}, E_{0e}, E_{0h} σ_{0e} and σ_{0h} are fixed parameters for band-tails of electron and hole states. The spontaneous emission rate then can be expressed as

$$r_{sp}(h\nu) = B(h\nu) \int \rho_e(E + h\nu) f_e(E + h\nu) \rho_h(E) f_h(E) dE \tag{1.35}$$

where *B* is the recombination coefficient, and $f_e(E)$, $f_h(E)$ are Fermi-Dirac distribution functions for electrons and holes. And the integration over energy has considered all possible transitions.

For the non-degenerate case, the Boltzmann approximation can be used for electron and hole occupations, i.e. $f_e(E) \cong \exp[(F_e - E)/k_B T]$ and $f_h(E) \cong \exp[(E - F_h)/k_B T]$, in which F_e and F_h are quasi-Fermi levels for electron and hole, respectively. Using this approximation, electron and hole distributions, N(E) and P(E) then can be given by

$$\begin{aligned} N(E) &= \rho_e(E) f_e(E, T, F_e) \\ &= \rho_{0e} \exp[(F_e - E_{0e}^*)/k_B T] \\ &\quad \times \exp(-\sigma_{0e}^2 / 2k_B^2 T^2) \\ &\quad \times \exp[-(E - E_{0e}^*)^2 / 2\sigma_{0e}^2] \end{aligned} \tag{1.36}$$

$$\begin{aligned} P(E) &= \rho_h(E) f_h(E, T, F_h) \\ &= \rho_{0h} \exp[(E_{0h}^* - F_h)/k_B T] \\ &\quad \times \exp(-\sigma_{0h}^2 / 2k_B^2 T^2) \\ &\quad \times \exp[-(E - E_{0h}^*)^2 / 2\sigma_{0h}^2] \end{aligned} \tag{1.37}$$

E_{0e}^{*} and E_{0h}^{*} are related to the central energies E_{0e} and E_{0h} of the corresponding tails via:

$E_{0e}^{*}=E_{0e}-\sigma_{0e}^{2}/k_BT$ and $E_{0h}^{*}=E_{0h}+\sigma_{0h}^{2}/k_BT$. Thus,

$$\begin{aligned} r_{sp}(h\nu) &= B\int N(E+h\nu)P(E)dE \\ &= B\rho_{0e}\rho_{0h}\exp[(F_e-E_{0e}^{*})/k_BT]\exp[(E_{0h}^{*}-F_h)/k_BT] \\ &\quad\times\exp(-\sigma_{0e}^{2}/2k_B^{2}T^{2})\exp(-\sigma_{0h}^{2}/2k_B^{2}T^{2}) \\ &\quad\times\int\exp[-(E+h\nu-E_{0e}^{*})^{2}/2\sigma_{0e}^{2}]\exp[-(E-E_{0h}^{*})^{2}/2\sigma_{0h}^{2}]dE \\ &= B\rho_{0e}\rho_{0h}\exp[(\Delta F-h\nu_0)/k_BT]\exp[(-\sigma_0^{2})/2k_B^{2}T^{2}] \\ &\quad\times\int\exp[-(E+h\nu-E_{0e}^{*})^{2}/2\sigma_{0e}^{2}]\exp[-(E-E_{0h}^{*})^{2}/2\sigma_{0h}^{2}]dE \end{aligned} \tag{1.38}$$

The convolution of a pair of Gaussian functions is also a Gaussian distribution with a sum of partial dispersions, so

$$r_{sp}(h\nu)\propto\exp[-(h\nu-h\nu_0)^{2}/2\sigma_0^{2}] \tag{1.39}$$

where $\Delta F=F_e-F_h$, $h\nu_0=E_{0e}^{*}-E_{0h}^{*}$ and $\sigma_0^{2}=\sigma_{0e}^{2}+\sigma_{0h}^{2}$.

The spontaneous emission spectrum thus is in Gaussian distribution with central peak given by

$$\begin{aligned} h\nu_0 &= E_{0e}^{*}-E_{0h}^{*}=E_{0e}-\sigma_{0e}^{2}/k_BT-E_{0h}-\sigma_{0h}^{2}/k_BT \\ &= E_0-\sigma_0^{2}/k_BT \end{aligned} \tag{1.40}$$

The quantity $E_0=E_{0e}-E_{0h}$ relates to the band gap E_g, and it follows the temperature dependence of the band gap, as described by the Varshini's equation mentioned earlier. The temperature dependence of the emission peak then can be expressed as:

$$d(h\nu_0)/dT=dE_g/dT+\sigma_0^{2}/k_BT^{2} \tag{1.41}$$

The second term on the right hand side in Eq. (1.41) can explain the anomalous blue shift with temperature, and the magnitude of this blue shift is related to the dispersion in the density of state.

For InGaN/GaN QWs, at sufficiently low temperatures, excitons tend to be localized in the potential minimal due to indium inhomogeneity. With increasing temperature, excitons become

more energetic, and are able to be excited from the localized band tail states to extended states. This thermal excitation can explain the well-observed blue shift in emission energy. However, when the temperature continues to increase, this band-tail-filling mode is not applicable due to strong degeneracy and a possible deviation from the quasi-equilibrium state.

1.6 THE PIEZOELECTRIC EFFECT

For a thin film of wurtzite InGaN grown on GaN along the *c*-axis (0001) direction, there exists a large piezoelectric field. This electric field is due to a high biaxial compressive strain in coherent growth, as well as large piezoelectric constants in the growth direction. The piezoelectric polarization in the growth direction can be expressed in terms of strain:[17]

$$P_3 = 2d_{31}\varepsilon_1(C_{11} + C_{12} - 2\frac{C_{13}^2}{C_{33}}) \tag{1.42}$$

where d_{31} is the piezoelectric modulus; C_{ik} is the elastic stiffness component; and ε_1 is the in-plane compressive strain.

In a quantum well structure, different piezoelectric and strain properties of well and barrier materials will result in different polarizations. This change of polarization is abrupt at the interface and introduces a fixed charge density in the neighborhood. Moreover, the accumulated charge at the interface will result in an electric field. For an arbitrary *n*-layer structure, two boundary conditions are assumed in order to calculate the electric fields induced by piezoelectric effect. One is that the electrical displacement vector is continuous at the adjacent interfaces; the other one is that the total potential drop across the structure is zero. Using these boundary conditions, the electric field is given as:

$$F_j = \frac{\sum_k (P_k - P_j)\frac{l_k}{\varepsilon_k}}{\varepsilon_j \sum_k \frac{l_k}{\varepsilon_k}} \tag{1.43}$$

where l_k and ε_k are the width and the electrical permittivity of the k_{th} layer, respectively.

To simplify the situation, we consider a single QW, and assume a uniform dielectric constant across the structure. The magnitude of the piezoelectric field is:

$$F_{w,b} = \frac{(P_{b,w} - P_{w,b})l_{b,w}}{\varepsilon(l_w + l_b)} \tag{1.44}$$

The electric fields in the well and barrier layer are of opposite sign, and the distribution of magnitude across the structure is proportional to the ratio of layer widths. Hence, a thin layer will have a higher electric field than a thick layer.

The energy band will be modified due to the presence of the piezoelectric field. This variation of band profile can be described by:

$$\begin{aligned} V(z) &= eF_b z + V_b, \text{ for } z < 0 \\ &eF_w z, \text{ for } 0 < z < l_w \\ &eF_b z + F_w l_w + V_b, \text{ for } z > l_w \end{aligned} \tag{1.45}$$

where l_w is the well width and V_b is the barrier height. Figure 1.6 shows the tilted band structure in anInGaN/GaN quantum well with a built-in electric field. The probability distributions for the ground state and the first excited state for electrons and holes are also shown. The electrons and holes are localized toward opposite sides in the quantum well.

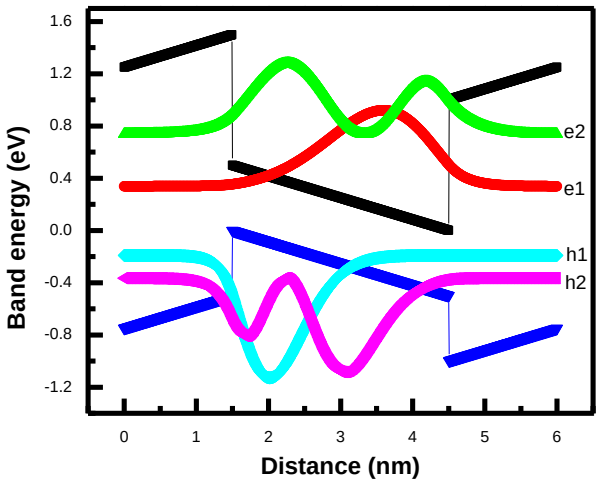

Fig. 1.7. Tilted band structure in an InGaN/GaN quantum well with a built-in electric field. The probability distributions for the ground state and the first excited state for electrons and holes are also shown. (Courtesy of Dr. Qiyuan Wei, a former group member)

The change of the band profile due to the piezoelectric field can have a significant impact on the emission properties. The well-known quantum confined Stark effect manifests itself as an decrease of the transition energy and a decrease of transition rate.[18-20] The later can be explained by the reduction of the dipole matrix element described in Eq. (1.32).

1.7 NONRADIATIVE RECOMBINATION

In addition to radiative recombination, electrons and holes can also recombine and convert energy to vibrational energy of lattice, i.e. phonons. This recombination mechanism is called non-radiative recombination, which reduces the emission efficiency and is unwanted in light emitting devices.

There are several possible mechanisms for non-radiative recombination in semiconductors, as shown in Fig. 1.8. A common mechanism is when recombination occurs at defects in the crystal structure, for example, dislocations, foreign atoms, or vacancies.[21,22] These defects have energy levels in the forbidden gap, and allow recombination through these energy levels, as shown in Fig. 1.8(a). Another important mechanism is Auger recombination shown in Fig. 1.8(b). The energy produced by electron-hole recombination is used to promote a free electron to a higher state in the conduction band, or a hole to deeper state in the valence band. Auger recombination is more pronounced at very high excitation densities.

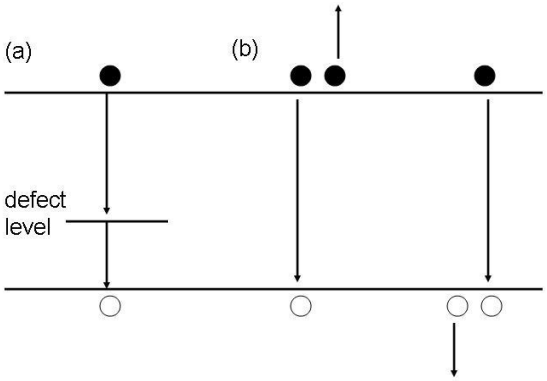

Fig. 1.8. Non-radiative recombination: (a) via a defect level, and (b) via Auger recombination.

In semiconductors with non-radiative recombination centers, the total probability of recombination is given by the sum of the radiative and non-radiative probabilities:

$$\tau^{-1} = \tau_r^{-1} + \tau_{nr}^{-1} \tag{1.46}$$

where τ_r is the radiative lifetime and τ_{nr} is the non-radiative lifetime. Thus, the internal quantum efficiency (the ratio of the number of photons emitted inside the semiconductor to the number of electrons injected into the semiconductor) is given by

$$\eta_{\text{int}} = \frac{\tau_r^{-1}}{\tau_r^{-1} + \tau_{nr}^{-1}} \tag{1.47}$$

In order to achieve high internal quantum efficiency, one possibility is to enhance the radiative recombination rate, and the other one is to decrease the non-radiative recombination rate.

1.8 LAYOUT OF THIS DISSERTATION

This dissertation investigates the optical properties of GaN and InGaN-based hetero-structures.

Chapter 2 reviews the main experimental technique, cathodoluminescence (CL), used during my doctorate program. The basic principle, experimental setup, and operation modes of cathodoluminescence are discussed therein. In addition, time-resolved CL is also discussed for the study of carrier dynamics. Examples of their applications on nitride semiconductors are presented as well.

Chapter 3 presents the study of strain effects on the optical emissions in GaN heteroepitaxial layers with different dislocation densities. It is combined with the microstructure study using a transmission electron microscope (TEM) and strain determination using x-ray diffraction. The dislocation densities are estimated for three epitaxial layers and the strain are also directly determined by measuring lattice parameter. The relationship between the emission energy of excitons and the in-plane compressive strain is demonstrated, and the emission energies increase with the residual strain.

In chapter 4, the fundamental optical transitions in cubic GaN and its temperature dependence are studied by cathodoluminescence. The excitonic transition, donor-acceptor pair recombination and its phonon replica are well resolved. The experimental results show that the ionization energies for both acceptors and donors are smaller than their counterparts in the wurtzite structure, which can contribute to efficient doping.

Chapter 5 presents the structural, optical, and electronic properties of blue, green, and yellow-emitting InGaN/GaN quantum wells (QWs). The effects of carrier localization, internal electrostatic fields, and non-radiative recombination on the light emission efficiency have been investigated. Carrier localization effects are manifested by compositional inhomogeneities, and temperature dependences of emission energies and radiative lifetimes. The electrostatic fields in the QWs, which results in long recombination lifetimes, are demonstrated in energy potential profiles. The effect of non-radiative recombination is also discussed regarding the emission efficiency.

Chapter 6 presents the effect of InGaN underlayers on the electronic and optical properties of visible InGaN/GaN quantum well structures. A significant improvement of the QW emission efficiency is observed as a result of the insertion of the $In_{0.03}Ga_{0.97}N$ underlayers, which is associated with a blue shift in the emission energy, a reduced recombination lifetime, an increased spatial homogeneity in the QW luminescence, and a weaker internal field across the QWs. These are explained by partial strain relaxation evidenced in the reciprocal space mapping of the X-ray diffraction intensity. Electrostatic potential profiles obtained by electron holography provide evidence for enhanced carrier injection by tunneling from the underlayer into the first QW.

In Chapter 7, the main findings of this dissertation are summarized and future work is suggested.

REFERENCES

1. I. Vurgaftman and J. R. Meyer, J. Appl. Phys. **94**, 3675 (2003).
2. M. P. Maruska and J. J. Tietjen, Appl. Phys. Lett. **15**, 327 (1969).
3. M. Ilegems and H. C. Montgomery, J. Phys. Chem. Solids. **34**, 885 (1973).
4. H. Amano, N. Sawaki, I. Akasaki, and Y. Toyoda, Appl. Phys. Lett. **48**, 353 (1986).
5. S. Nakamura, Jpn. J. Appl. Phys. **30**, L1705 (1991).
6. H. Amano, M. Kito, K. Hiramatsu, and I. Akasaki, Jpn. J. Appl. Phys. **28**, L2112 (1989).
7. S. Nakamura, M. Senoh, and T. Mukai, Jpn. J. Appl. Phys. **30**, L1708 (1991).
8. M. Suzuki, T. Uenoyama, and A. Yanase, Phys. Rev. B **52**, 8132 (1995).
9. S. L. Chuang, "Physics of Optoelectronic Devices", (Wiley, New York, 1995), pp 337-344.
10. Y. P. Varshni, Physica **34**, 149-54 (1967).
11. S. Chichibu, T. Azuhata, T. Sota, and S. Nakamura, J. Appl. Phys. **79**, 2784-6 (1996).
12. Y.-H. Cho, G. H. Gainer, A. J. Fischer, J. J. Song, S. Keller, U. K. Mishra, and S. P. DenBaars, Appl. Phys. Lett. **73**, 1370 (1998).
13. H. P. D. Schenk, M. Leroux, and P. de Mierry, J. Appl. Phys. **88**, 1525 (2000).
14. J. Li, K. B. Nam, J. Y. Lin, and H. X. Jiang, Appl. Phys. Lett. **79**, 3245 (2001).
15. A. Bell, S. Srinivasan, C. Plumlee, H. Omiya, F. A. Ponce, J. Christen, S. Tanaka, A. Fujioka, and Y. Nakagawa, J. Appl. Phys. **95**, 4670-4 (2004).
16. P. G. Eliseev, P. Perlin, J. Lee, and M. Osinski, Appl. Phys. Lett. **71**, 569-71 (1997).
17. J. F. Nye, "Physical Properties of Crystals: Their Representation by Tensors and Matrices", (Oxford, Clarendon Press, London, 1985), pp 124-141.
18. T. Takeuchi, S. Sota, M. Katsuragawa, M. Komori, H. Takeuchi, H. Amano, and I. Akasaki, Jpn. J. Appl. Phys. **36**, L382 (1997).
19. J. S. Im, H. Kolmer, J. Off, A. Sohmer, F. Scholz, and A. Hangleiter, Phys. Rev. B **55**, R9435 (1998).
20. C. Wetzel, T. Takeuchi, H. Amano, and I. Akasaki, Phys. Rev. B **62**, R13302 (2000).
21. S. J. Rosner, E. C. Carr, M. J. Ludowise, G. Girolami, and H. I. Erikson, Appl. Phys. Lett. **70**, 420 (1997).

22. T. Koida, S. F. Chichibu, A. Uedono, A. Tsukazaki, M. Kawasaki, T. Sota, Y. Segawa, and H. Koinuma, Appl. Phys. Lett. **82**, 532 (2003).

CHAPTER 2

EXPERIMENTAL TECHNIQUES

2.1 CATHODOLUMINESCENCE SPECTROSCOPY AND IMAGING

Cathodoluminescence (CL) refers to the emission of light which results from the interaction of an electron beam with a specimen. When an electron beam is bombarded onto a material, part of the incident energy excites valence electrons in the material to higher energy states in the conduction band. This promotion will create free electron-hole pairs, and subsequent radiative recombination of these pairs leads to characteristic light emission.

The electron beam energy dissipation and the corresponding excitation volume in the material can be described using analytical approximations. The effective depth to which energy dissipation extends in the material is known as the Gruen range, or penetration range. This penetration range is important to us in view of CL analysis. The Gruen range of the electron penetration is a function of the electron beam energy E_b, $R_e = (k/\rho)E_b^{\alpha}$, where ρ is the density of the material, k and α depend on the atomic number of the material and also the electron beam energy.[1] A more general model derived by Kanaya and Okayama gives the penetration range as:[2]

$$R_e = (0.0276A/\rho Z^{0.889})E_b^{1.67}(\mu m) \qquad (2.1)$$

where ρ is material density in g/cm^3 ; E_b is electron beam energy in keV; A is the atomic weight in g/mol; and Z is the atomic number. The penetration range as a function of the electron beam energy for GaN using this model is shown in Fig. 2.1, in which A is 83.73g/mol and ρ is 6.15 g/cm^3. The sum of atomic numbers of Ga and N (Z=38) is used in Eq. (2.1). This dependence of penetration range provides a capability for depth-resolving in CL using various electron beam energy. However, special attention has to be paid on the influence of accelerating voltage on quality of images taken by scanning electron microscope. At higher accelerating voltages, the

beam penetration and diffusion areas become larger, resulting in unnecessary signals (like back-scattered electrons). These signals can reduce the image contrast and veil the fine sample surface structure. Thus, we need to carefully choose accelerating voltage for different purposes.

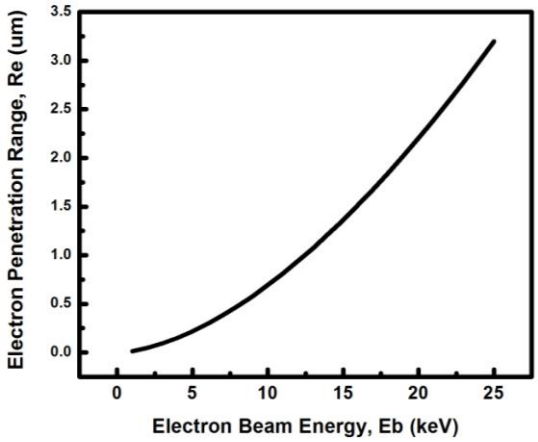

Fig. 2.1. The penetration range as a function of the electron beam energy for GaN using Eq. (2.1).

Figure 2.2 shows an example of depth-resolved spectra for an LED structure (using InGaN/GaN QWs in the active region, and *p*-type and *n*-type GaN cladding the active region as waveguides). When the electron beam, with accelerating voltages of 5 kV and 8 kV excite the structure, only the emission peak associated with defects in Mg doped GaN is observed, which means the electron beam excites mostly the top *p*-type region. By increasing electron beam energy, the emission from the QWs emerges at about 12 kV, followed at even higher beam energy by the emission from the underneath GaN layer.

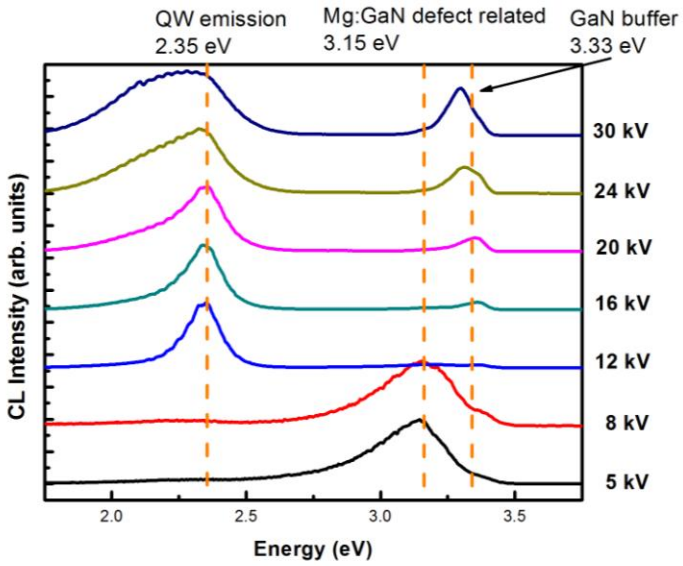

Fig. 2.2. An example of depth-resolved spectra for an LED structure. Emissions from different layers can be resolved by varying accelerating voltage of the electron beam.

Another advantage of the cathodoluminescence is that it has the ability to focus to very small spots, about 3-5 nm in size, which gives us the possibility to detect spatial variations of the luminescence. Figure 2.3(b) shows the emission spectra taken at different locations, marked in Fig. 2.3(a), on a cross section GaN film grown by the ammonthermal technique. This result has been published in Ref. 3. The grown crystal has strong near band edge peak at 3.41 eV, with a very low blue-yellow luminescence. However, the interfaces between the seed and the new growth (areas 4 and 6) have strong yellow luminescence. Note that the blue luminescence in area 4 may contain either more impurities or more defects than in area 6. From these patterns, one can find that the crystal quality improves with growth. The strong near band edge peaks at 3.41 eV measured at areas 1 and 2 are similar to the one at area 5 (seed), and the yellow and blue bands decrease as the crystal grows thicker. It has been reported that impurities, native point defects, and dislocations could all be the sources of the yellow luminescence.[4,5]

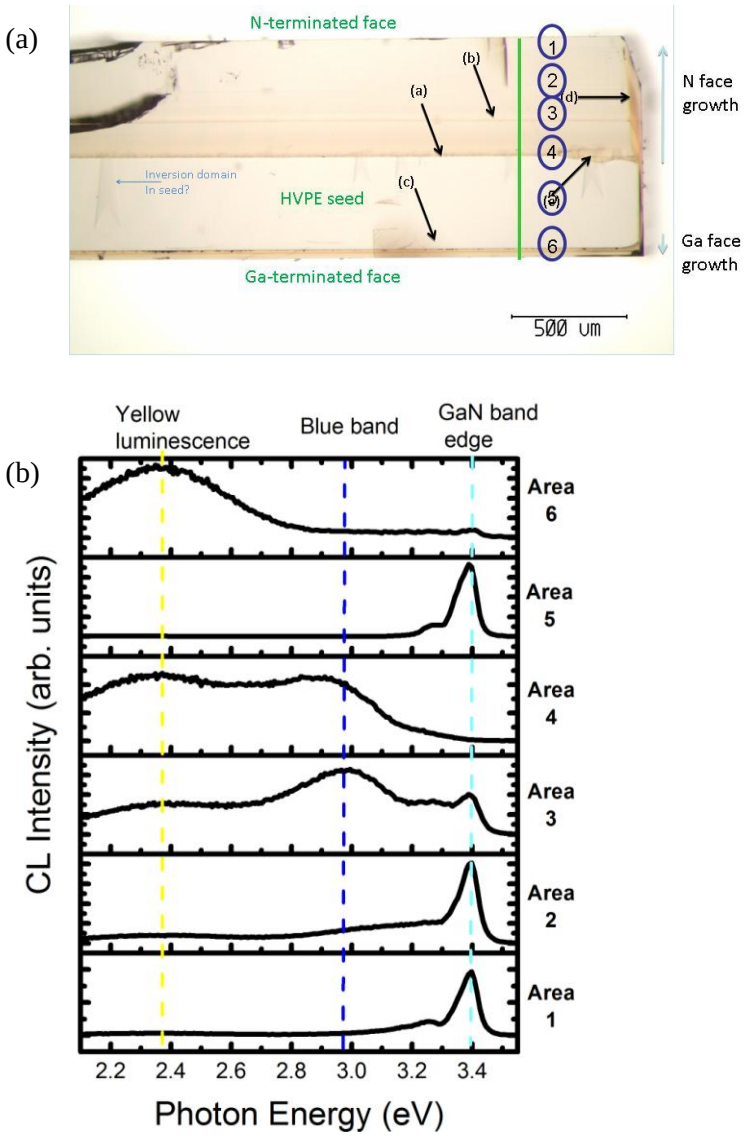

Fig. 2.3. (a) Cross section image of ammonothermal GaN crystal; (b) CL spectra taken at different locations in the cross section marked in (a) to compare the seed, the nitrogen terminated face and galium terminated face.

Moreover, a large number of CL spectra taken at different spatial locations can be put together to generate CL images of luminescence. Figure 2.4 shows a CL image of a-GaN grown on patterned *r*-sapphire substrate. The monochromatic CL image is produced by setting the spectrometer at the wavelength of GaN band edge emission peak, and luminescence intensities are recorded at different locations by raster scan. Plan view scanning electron microscope image of the patterned *r*-plane sapphire substrate is shown in Fig. 2.4(a). The hemisphere array is

uniform in size and arranged in hexagonal symmetry. The monochromatic CL image in Fig. 2.4(b) exhibits inhomogeneous features with dimensions and morphology similar to that of the patterned substrate: some round areas distributed in a hexagonal symmetry appear bright and are bounded by dark regions. It should be noted that because of a limited spatial resolution of CL caused by relatively large excitation volume and diffusion length, the boundary of emission pattern is not sharp, and the size of the bright regions appear larger than of the hemisphere dimensions. This result has been published in Ref. 6.

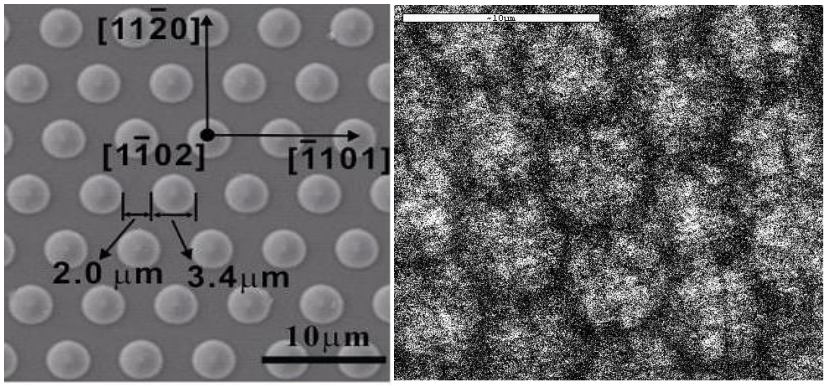

(a) **(b)**

Fig. 2.4. (a) Plan view scanning electron microscope image of the patterned r-plane sapphire substrate; (b) CL image taken at the GaN band edge emission.

Figure 2.5 shows the CL set up installed in a scanning electron microscope, a JEOL 6300 equipped with a LAB_6 thermionic electron gun, which provides us a convenient mean of excitation. The electron beam tilt and shift are controlled by the condenser lenses. The light emitted from the samples will be reflected towards a movable parabolic mirror on top of the sample stage. The sample surface is adjusted to the focal point of the mirror for maximum light collection. The mirror contains a pinhole in the center, which allows the electron beam probe to pass through, scan, and excite the sample. The reflected light transmitting through a slit will be analyzed by a spectrometer and then detected by photomultiplier tube.

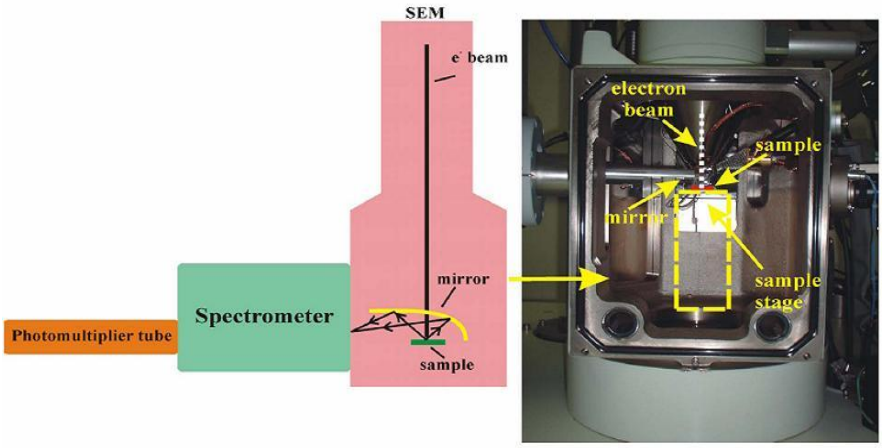

Fig. 2.5. The CL set up installed in a scanning electron microscope. CL measurements are facilitated by additional equipment, which consists of a parabolic mirror, the spectrometer, and the detector.

2.2. TIME-RESOLVED CATHODOLUMINESCENCE

Time-resolved CL measurement can provide more quantitative information about minority carriers. In particular, the minority carrier lifetime can be derived from the temporal dependence of the CL intensity.

In time-resolved CL, the precise time measurement is extremely important. Time-correlated single photon counting (TCSPC) is used to measure the arrival time of each individual photon.[7] We deal with a detector signal which is a train of randomly distributed pulses corresponding to the detection of the individual photons. There are many signal periods without photons; other signal periods contain one photon pulse. Periods with more than one photon are very rare. The TCSPC technique makes use of this fact that for low-level, high-repetition-rate signals, the light intensity is so low that the probability of detecting one photon in one single period is far less than one. Therefore, it is not necessary to provide for the possibility of detecting several photons in one single period. It is sufficient to record the photons, measure their time in a single period, and build a histogram of the photon times. When a photon is detected, the time of the corresponding detector pulse in the signal period is measured. The events are collected in a memory by adding a

"1" in a memory location with an address proportional to the detection time. After many photons, the distribution of the detection times builds up in the memory.

This method requires blanking of the electron beam so that it strikes the sample for certain fixed intervals of time. This is achieved by blanking plates installed in the path of electron beam, which are connected to a pulse generator. The frequency of the electron beam pulse can be adjusted from 1 kHz to 1 MHz. The pulse rise and fall times were below 100 ps with an overall system resolution under 400 ps measured with a GaAs photocathode detector. The time resolution of our system makes it situable for the measurement of lifetime for InGaN QW structures. The time of detection of a photon is measured from the reference pulse from the excitation source, which demonstrates the time dependence of light emission. Figure 2.6 shows a typical temporal dependence of CL intensity, which is called a transient. When the electron beam is switched on, the luminescence intensity builds up, eventually reaching a quasi-steady state. And after the electron beam is switched off, the decay in luminescence is observed. The recombination lifetime τ can be extracted from the transient by fitting the luminescence decay with a single exponential function.

$$I(t) = I_0 \exp(-t/\tau) \tag{2.2}$$

where I_0 represents the intensity when the beam is just switched off.

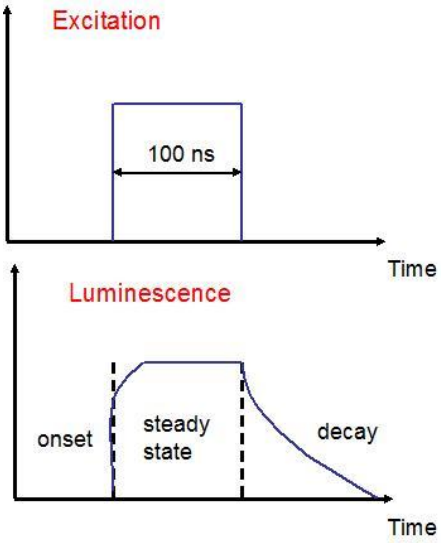

Fig. 2.6. Schematic pulsed excitation and corresponding temporal dependence of luminescence intensity. The frequency of the electron beam can vary from 1 kHz to 1 MHz. The turn on and turn off time for the electron beam is less than100 ps.

In addition, transients taken at different wavelengths can be put together and form time-resolved CL spectra. Figure 2.7 shows the time-resolved CL spectra for InGaN QW structures emitting at 465 nm. The QWs demonstrate a redshift after the electron beam is switched off. This redshift can be explained either by band empty effect, or a restored electric field due to the decrease in excitation density.

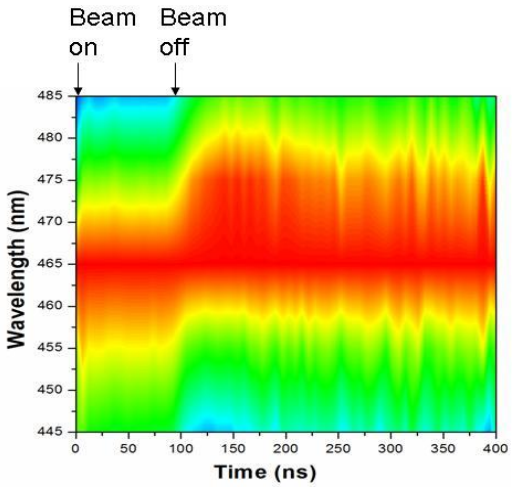

Fig. 2.7. Time-resolved CL spectra for InGaN QW structures emitting at 465 nm. The QWs demonstrate a redshift after the electron beam is switched off.

REFERENCES

1. T. E. Everhart and P. H. Hoff, J. Appl. Phys. **42**, 5837 (1971).

2. K. Kanaya and S. Okayama, J. Phys. D **5**, 43 (1972).

3. B. Wang, D. Bliss, M. Suscavage, S. Swider, R. Lancto, C. Lynch, D. Weyburne, T. Li, and F. A. Ponce, J. Cryst. Growth, **318**, 1030 (2011).

4. T. Ogino, and M. Aoki, Jpn. J. Appl. Phys. **19**, 2395 (1980).

5. J. Neugebauer and C. G. VandeWalle, Appl. Phys. Lett. **69**, 503 (1996).

6. Z. H. Wu, Y. Q. Sun, J. Yin, Y.-Y Fang, J. N. Dai, C. Q. Chen, Q. Y. Wei, T. Li, K. W. Sun, A. M. Fischer, and F. A. Ponce, J. Vac. Sci. Technol. B **29**, 021005 (2011).

7. W. Becker, "Advanced Time-Correlated Single Photon Counting Techniques", (Springer, Berlin, 2005).

CHAPTER 3

DISLOCATION DENSITY AND STRAIN EFFECTS IN GAN EPITAXY ON SAPPHIRE

A study is reported on the effect of dislocation density and residual strain on the light emission characteristics of GaN epilayers grown on sapphire. A linear relationship is demonstrated between the exciton emission energy and the in-plane compressive strain calculated with respect to the epilayer which has highest dislocation density. It shows that the exciton emission energy increases with the magnitude of the in-plane compressive strain. This study was carried out by a combination of transmission electron microscopy (TEM), x-ray diffraction (XRD), cathodoluminescence (CL) and photoluminescence (PL) spectroscopy. The dislocation densities and the lattice parameters in the low temperature buffer layer are determined TEM. The lattice parameters of the GaN epitaxial layers are obtained by XRD.

3.1 INTRODUCTION

Heteroepitaxial growth involves deposition of a film on a substrate, typically encountering lattice and thermal-expansion mismatch. In the early history of growth of GaN, the films were composed of sub-micrometer crystalline grains and rough surfaces. The problem was solved by the use of low-temperature (~500℃) thin buffer layers, which is also known as nucleation or wetting layer.[1,2] This is followed by growth of GaN layer at high temperatures (typically ~ 1000℃). At the beginning of the high-temperature growth, GaN islands nucleate on the buffer layer. The island nucleation density is related to the numbers of dislocations. These islands coalesce subsequently and eventually result in a flat surface. GaN epilayers grown on sapphire substrates are characterized by dislocation densities up to 10^{10} cm^{-2}.[3] Growth conditions in the early stage of high-temperature growth are critical for controlling dislocation densities. In addition, the thermal expansion characteristics of GaN differ significantly from sapphire.[4] The consequent thermal stress that develops during cooling down from the high growth temperature can generate high levels of strain in the film. Due to the low crystal quality of the buffer layer, it is difficult to observe misfit dislocation at the interface, hence threading dislocation is an indicator for strain relaxation and epilayer quality.

The aim of this study is the determination of the dislocation densities, residual strain and their effects on the optical properties. The dislocation densities and the lattice parameters in the low temperature buffer layer are determined by high-resolution transmission electron microscopy (TEM) images. The in-plane strain in the GaN epitaxial layers are calculated with respect to the epilayer which has the highest dislocation density, using lattice parameters obtained by x-ray diffraction (XRD). Furthermore, the relationship between the emission energy of excitons and the in-plane compressive strain is demonstrated.

3.2 EXPERIMENTAL DETAILS

The GaN epilayers were grown by metal-organic chemical vapor deposition on (0001) sapphire substrates. A low-temperature buffer layer technique was used in the growth: after proper pretreatment of the sapphire substrate, a very thin GaN buffer layer was deposited at relatively low-temperatures (LT, 500-600℃) to provide adequate nucleation sites.[1, 2] Then the growth temperature was ramped up to 900-1200℃ to anneal the LT buffer layer and then deposit a thick GaN epilayer. Generally the structural characteristics of the thick GaN epilayer is determined by various growth parameters such as temperature, pressure, V/III ratio, and buffer layer thickness.[2] We have obtained three GaN epilayers with different dislocation density to study the residual strain and related effects.

The threading dislocation densities and residual strain in the GaN epilayers are characterized by TEM and XRD measurements. The light emission characteristics are evaluated by cathodoluminescence (CL). Cross-sectional thin TEM specimens were prepared using standard mechanical polishing and argon-ion milling techniques. The microstructure was studied using a field-emission TEM with incident electron beam energy of 200 keV. CL spectra were obtained at liquid-helium temperature in a scanning electron microscope operated at an electron acceleration voltage of 5kV.

3.3 STRUCTURAL PROPERTIES

Figure 3.1 shows cross-sectional TEM images for the three GaN epilayers. A diffraction condition g = [11-20] in Fig. 3.1 is chosen so that only dislocations with an edge component are visible. From TEM images taken with g = [0002] which are not shown here, we can conclude that more than 80% of the dislocations have an edge components (edge- or mixed- dislocation types). The thickness of the TEM specimen was determined by convergent beam electron diffraction (CBED) technique in order to estimate the threading dislocation density (TDD). The regions shown in Fig. 3.1 have a similar thickness (~ 200 nm ± 15%), so the TDD for three

epilayers can be compared directly. The TDD in epilayer # 1 is about one order of magnitude lower than epilayer # 2, and two orders of magnitude lower than epilayer # 3. By averaging over a large area, the TDD in samples 1, 2, and 3 were estimated to be $4.5\times10^{7}/cm^{2}$, $5.0\times10^{8}/cm^{2}$, and $5.0\times10^{9}/cm^{2}$, respectively.

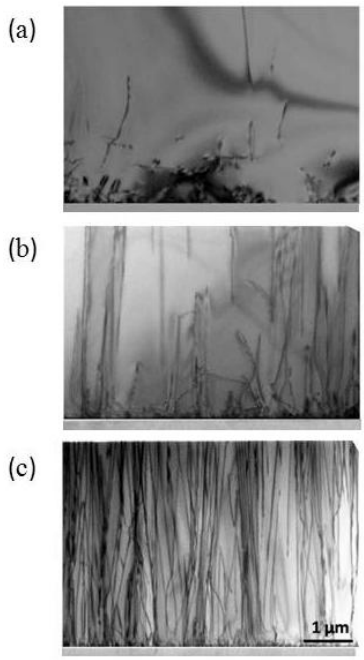

Fig. 3.1. Cross-sectional TEM images of three GaN epilayers with increasing dislocation density from (a) to (c). The diffraction condition chosen is g = [11-20].

In addition, lattice parameters can be determined by high-resolution TEM images. A typical lattice image including the sapphire/LT GaN buffer layer interface and its Fourier transformed image are shown in Fig. 3.2. By counting the average number of substrate fringes nave between two terminating fringes at the interface in the Fourier transformed image, we can obtain the lattice parameter ae using the following equation:

$$n_{ave}(a_e - a_s) = a_e \qquad (3.1)$$

where a_s is the lattice parameter of the substrate. Therefore, the lattice parameters in the LT buffer layer are determined to be a_e=3.145 for epilayer #1 and a_e=3.163 for epilayer #3.

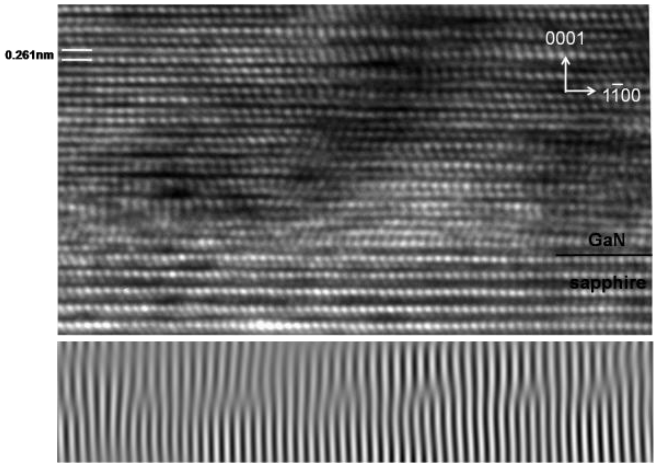

Fig. 3.2. High-resolution lattice image of region that includes the interface between sapphire and the low-temperature GaN buffer layer interface (top). A Fourier transformed image of the interface region is shown (bottom).

The state of the strain in the HT GaN epitaxial layer differs from the state in the LT buffer layer. Determination of in-plane strain in the epitaxial layer requires measuring the lattice parameter a using XRD. This can be achieved by measuring the interplanar spacing *d* for (002) and (105) planes. The interplanar spacing for (*hkl*) planes in wurtzite structure are expressed as

$$d_{hkl} = \sqrt{\frac{1}{(h^2+k^2+hk)\frac{4}{3a^2}+\frac{l^2}{c^2}}} \qquad (3.2)$$

Figure 3.3 shows XRD 2θ scan for the (002) and (105) diffraction spots of the three epitaxial layers, and the interplanar spacing d_{002} and d_{105} are determined from the peak position in the 2θ scan using Bragg's law:

$$2d\sin\theta = \lambda \qquad (3.3)$$

Then the lattice parameter *c* and *a* are obtained using Eq. (3.2), are shown in table 3.1. The values for epilayer # 3 which has the highest dislocation density, are close to the values obtained for high-purity GaN powder by Reeber.[5] Thus, the epilayer #3 can be considered relaxed, and the strains in the epilayers #1 and 2 are calculated with respect to epilayer #3. The in-plane strain can be calculated using the following equation:

$$\varepsilon_{xx} = \frac{a_e - a_r}{a_r} \qquad (3.4)$$

where a_r is the lattice parameter for relaxed material, using the value of epilayer #3. The weak diffraction of the (105) planes can introduce a large uncertainty in determining the lattice parameter *a* and the strain calculated using Eq. (3.4). The other approach is using lattice parameter c and the relationship between the in-plane and perpendicular strains as follow:

$$\varepsilon_{zz} = \frac{c_e - c_r}{c_r}$$

$$\varepsilon_{xx} = -\frac{C_{33}}{2C_{13}}\varepsilon_{zz} \qquad (3.5)$$

C_{13}= 98 GPa and C_{33}= 389 GPa are used in the above equation.[6] The in-plane strain values obtained are also shown in Table 3.1. These values are one order of magnitude lower than the values determined in the LT buffer layer using high-resolution TEM.

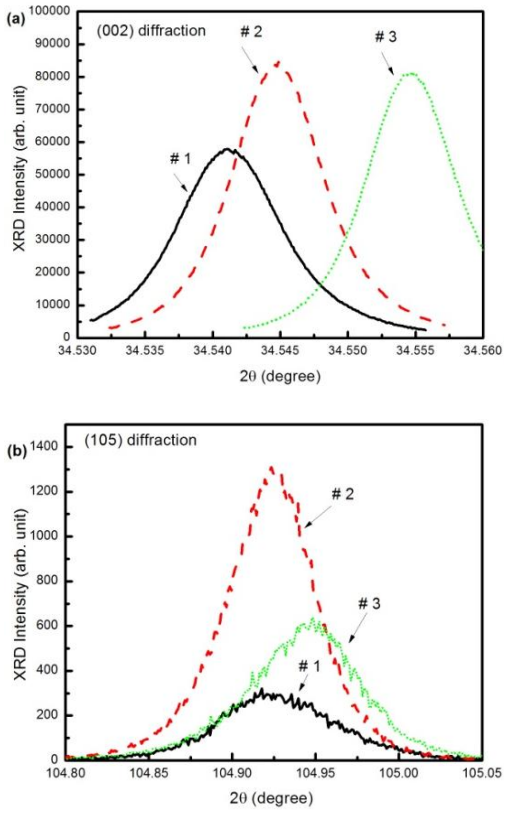

Fig. 3.3. XRD θ–2θ scan for (a) (002) diffraction spot and (b) (105) diffraction spot of the three epitaxial layers. Lattice parameter *a* and *c* can be obtained from the peak position using Eq. (3.4) and (3.5).

TABLE 3.1. Lattice parameters and in-plane strain for three epilayers. The lattice parameters are in angstrom units. In the case of GaN film, the strain is determined from the *c*-parameter measured using x-ray diffraction data and the poisson ratio. In the case of the GaN buffer layer, the strain is directly determined from the *a*-period in TEM lattice fringes.

Epilayer	Dislocation Density	Lattice parameter *a*	Lattice parameter *c*	Strain
1	$4.5\times10^{7}/cm^{2}$	3.1866	5.1892	-0.075%
2	$5.0\times10^{8}/cm^{2}$	3.1894	5.1886	-0.054%
3	$5.0\times10^{9}/cm^{2}$	3.1919	5.1872	0
Reeber[6]	0	3.19091	5.18796	
Buffer layer in sample 1		3.145		-0.147%
Buffer layer in sample 3		3.163		-0.091%

3.4 OPTICAL PROPERTIES

Figure 3.4(a) shows the liquid helium temperature CL spectra for nominally undoped GaN epilayers with increasing dislocation densities. For all three samples, the spectra are dominated by sharp and strong excitonic emissions around 3.5 eV. Phonon replicas separated by 92 meV from the central excitonic emission are also observed. In addition, a weak but wide blue band emission around 3.0 eV is present due to residual deep acceptor levels.[7, 8] The intensities of all emissions decrease with the dislocation densities. The dominant excitonic emissions have characteristic fine structures, and there are also slight energy shifts among the epilayers with different dislocation densities. To investigate the effects of dislocation densities on the optical properties, a close-up of excitonic emissions is shown in Fig. 3.4(b). The positions of neutral donor bound exciton (I_2), free *A* exciton (*A* (n=1)), free *B* exciton (*B* (n=1)), and the first excited states of the donor bound exciton and the *A* exciton (I_2 (n=2) and *A* (n=2)) are marked for the first sample. The other two epilayers both maintain the similar emission features. The emission peaks red-shift with increasing dislocation density.

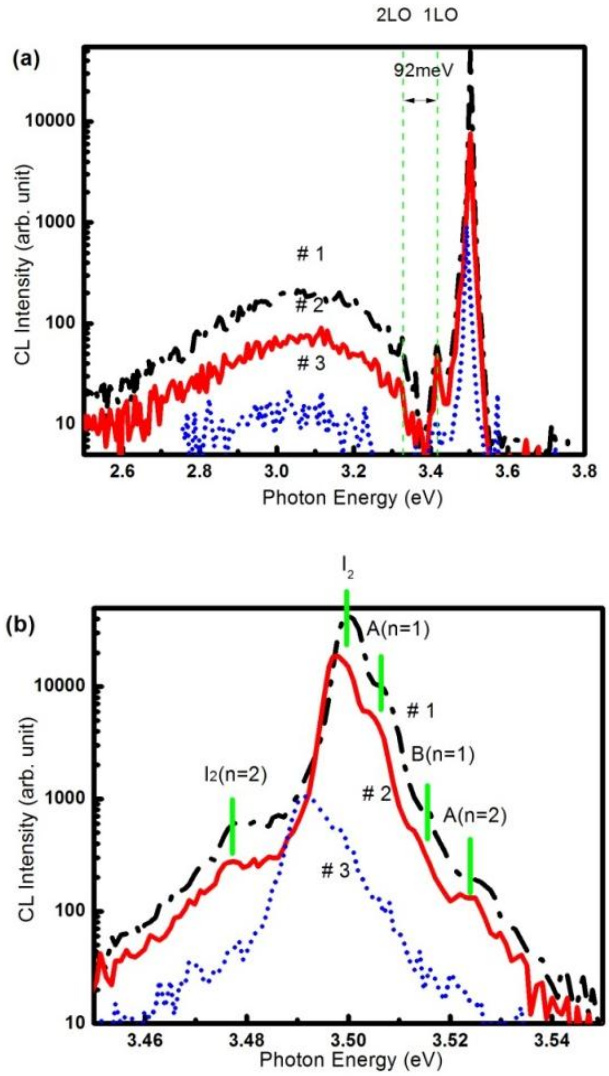

Fig. 3.4. (a) The low-temperature CL spectra of three epilayers from # 1 to # 3 with increasing dislocation densities. The vertical dash lines indicate the positions of phonon replicas. (b) A close-up of the dominant excitonic emissions for these three epilayers. Neutral donor bound exciton (I_2), free *A* exciton (*A* (n=1)), free *B* exciton (*B* (n=1)), and the first excited states of the donor bound exciton and the *A* exciton (I_2 (n=2) and *A* (n=2)) are marked.

We plot in Fig. 3.5 the emission energies of the *A*, *B*, and bound excitons as a function of the fundamental *A* transition. The energy of the *A* exciton is considered to be an intrinsic feature of each epilayer. In addition to our measurements, other data reported for epilayers with various thicknesses, or on different substrates, or using different growth techniques, are also plotted for a comparison.[9-14] Those emission energies can be found in Table 3.2. Despite a large discrepancy among the reported values, there is clear linear relationship between the emission energies and

the fundamental *A* transition. This experimental evidence can indicate the influence of dislocation density on the emission energy, which is attributed to the residual strain in the epilayer.

TABLE 3.2. Low-temperature values (<10 K) reported for transition energies of wurtzite GaN epilayer.

Reference #	*A* exciton (eV)	*B* exciton (eV)	Bound exciton (eV)	Thickness (*u*m)
9	3.4745	3.4805	3.467	150
10	3.4751	3.4815	3.469	110
11	3.485	3.493	3.479	4
12	3.4775	3.4845		4
13	3.4799	3.4860	3.4727	400
13	3.4962	3.5050	3.4900	3
14	3.4770	3.4865	3.471	not communicated

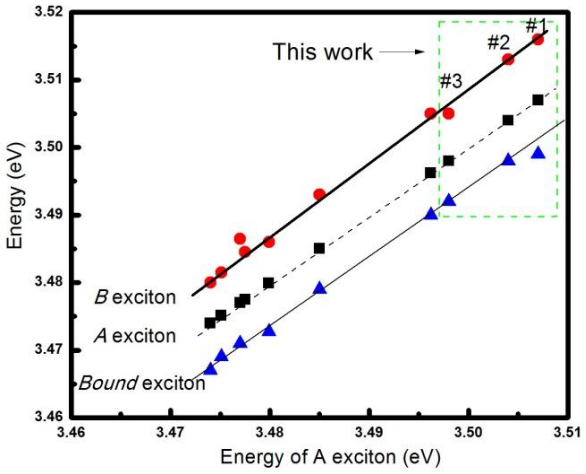

Fig. 3.5. Emission energies of the *A*, *B*, and bound excitons vs the *A* transition. Data in the box are experimental results of this work.

The relationship between exciton emission energy and strain is shown in Fig. 3.6. The strain values are calculated using Eq. (3.5). It is clear that the exciton emission energy increases linearly with the magnitude of the in-plane compressive strain. The slopes of the linear fitting are also

shown in Fig. 3.6, and they can be defined as "effective deformation potentials". These effective deformation potentials describe the relationship between the emission energy shift with strain. The effective deformation potential is 11.8 eV for *A* exciton, 14.7 eV for *B* exciton and 9.7 eV for bound exciton.

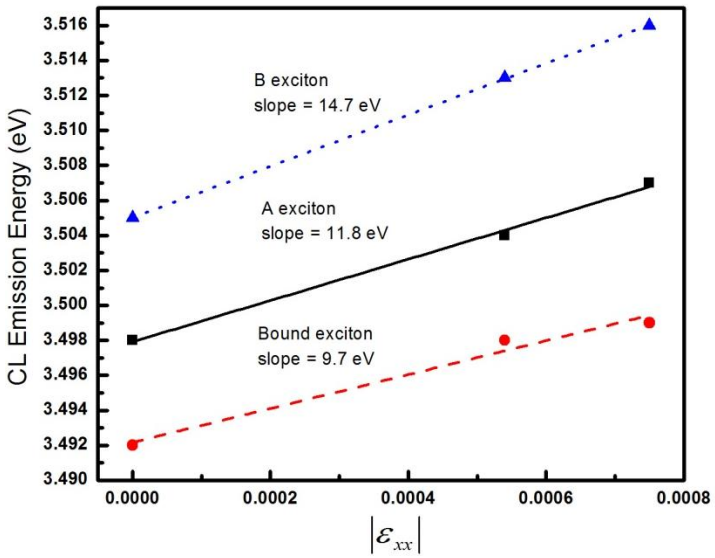

Fig. 3.6. Relationship between the exciton emission energies and the in-plane compressive strain. The slopes of the linear fitting are defined as effective deformation potentials.

3.5 PHOTOLUMINESCENCE RESULTS

Figure 3.7(a) shows photoluminescence (PL) spectra for the three epilayers taken at a temperature of 10 K. A 325-nm HeCd laser with an average power of 60 μW is used for excitation. Similar to the CL spectra, a redshift in the band-edge emission energy with increasing dislocation density is observed. The positions of the neutral donor bound exciton (I_2), free *A* exciton (*A* (n=1)), and free *B* exciton (*B* (n=1)) are marked for each epilayer, except that *B* exciton is not distinguishable in epilayer # 3. The peak energies are obtained by Gaussian fittings with an uncertainty of ~ 0.2 meV, and they are plotted vs the strain in Fig. 3.7(b). The deformation potentials obtained by the linear fitting are 9.8 eV for *A* exciton, and 12.6 eV for bound exciton.

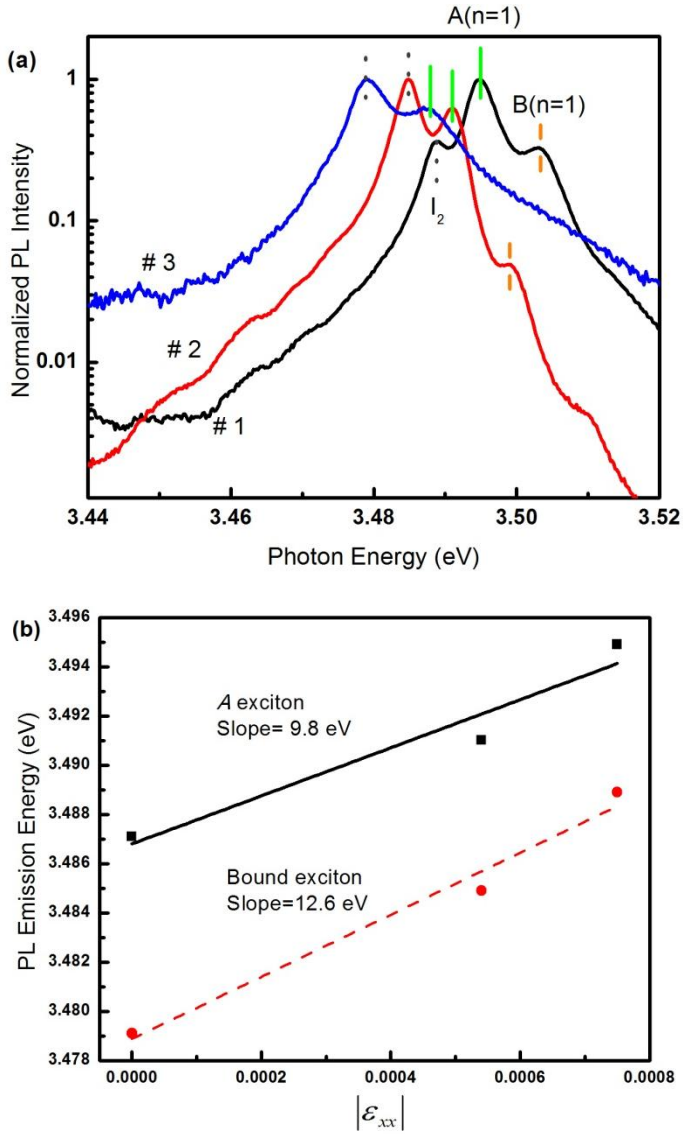

Fig. 3.7. (a) Photoluminescence (PL) spectra for the three epilayers taken at a temperature of 10 K. The positions of the neutral donor bound exciton (I_2) are marked with dot lines; the positions of the free *A* exciton (*A* (n=1)) are marked with solid lines; and the positions of the free *B* exciton (*B* (n=1)) are marked with dash lines. (b) The relationship between the PL emission energies and the strain.

Figure 3.8(a), (b), and (c) show comparisons between the PL and CL spectra for the epilayers # 1, # 2, and # 3, respectively. We observe a redshift in the emission energy and an increase in the peak width. The increase in the peak width may be due to a deeper penetration depth of photon excitation (~ 1-10 μm) than the electron beam (~ 200 nm at 5 kV). Therefore, PL can pick up signal from the regions close to the buffer layer where the material quality is not as

good as regions close to the surface. This may also contribute to the different deformation potentials extracted from PL measurements.

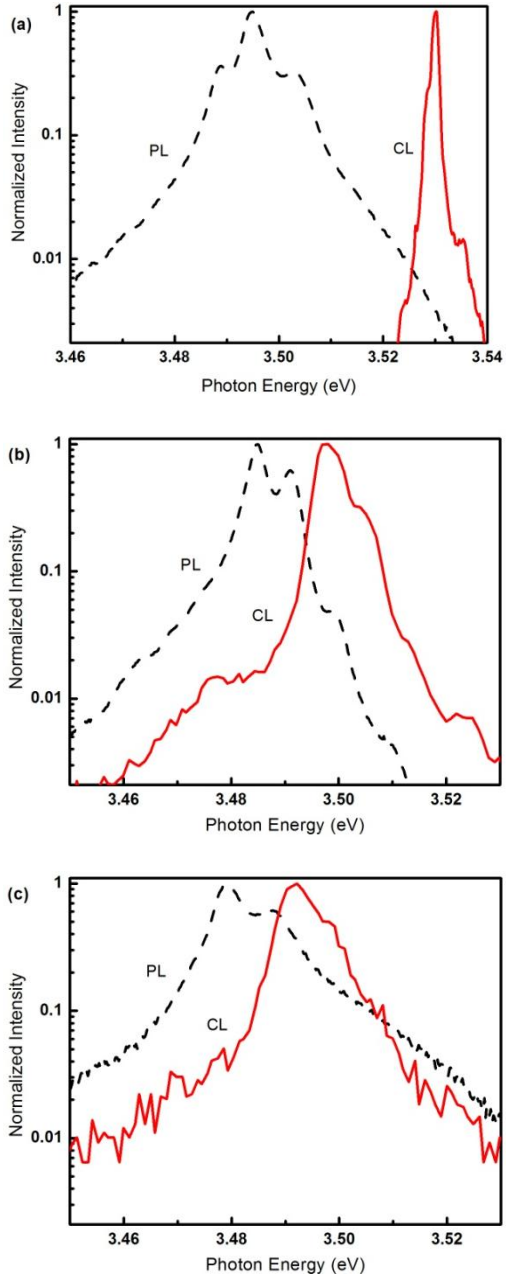

Fig. 3.8. Comparisons between the PL and CL spectra for (a) the epilayer # 1, (b) the epilayer # 2, and (c) the epilayer # 3.

3.6 SUMMARY

The structural and optical properties of GaN epitaxial layers with different dislocation densities are examined by transmission electron microscopy, X-ray diffraction, cathodoluminescence and photoluminescence spectroscopy. The values of dislocation densities are obtained from cross-sectional TEM micrographs, and the lattice parameters in the low-temperature GaN buffer layer are obtained by high-resolution lattice image. The lattice parameters in the GaN epitaxial layers are obtained by XRD measurement. The in-plane strain with respect to the epilayer which has the highest dislocation density are determined, which is about one magnitude lower than the value for the buffer layer. It is also shown that the exciton emission red shifts with increasing dislocation density, and increases with the magnitude of the in-plane compressive strain. Using emission energies from CL measurements, an effective deformation potential has been defined to demonstrate the strain effects on the exciton emission energy shift, which is 11.8 eV for *A* exciton, 14.7 eV for *B* exciton and 9.7 eV for bound exciton. The deformation potentials using PL emission energies are 9.8 eV for *A* exciton, and 12.6 eV for bound exciton.

REFERENCES

1. H. Amano, N. Sawaki, I. Akasaki, and Y. Toyoda, Appl. Phys. Lett. **48**, 353 (1986).

2. S. Nakamura, Jpn. J. Appl. Phys. **30**, L1705 (1991).

3. S. D. Lester, F. A. Ponce, M. G. Craford, and D. A. Steigerwald, Appl. Phys. Lett. **66**, 1249 (1995).

4. M. Leszczynski, T. Suski, H. Teisseyre, P. Perlin, I. Grzegory, J. Jun, S. Porowski, and T. D. Moustakas, J. Appl. Phys. **76**, 4909 (1994).

5. R. R. Reeber, and K. Wang, J. Materials Research, **15**, 40 (1999).

6. J.-M. Wagner and F. Bechstedt, Phys. Rev. B **66**, 115202 (2002).

7. M. Toth, K. Fleischer, and M. R. Phillips, Phys. Rev. B **59**, 1575 (1999).

8. M. A. Reshchikov, F. Shahedipour, R. Y. Korotkov, M. P. Ulmer, and B. W. Wessles, Physica B **105**, 273 (1999).

9. R. Dingle, D. D. Sell, S. E. Stokowski, and M. Ilegems, Phys. Rev. B **4**, 1211 (1971).

10. B. Monemar, Phys. Rev. B **10**, 676 (1974).

11. W. Shan, T. J. Schmidt, X. H. Yang, S. J. Hwang, and J. J. Song, Appl. Phys. Lett. **66**, 985 (1995).

12. B. Gil, O. Briot, and R.-L. Aulombard, Phys. Rev. B **52**, R 17028 (1995).

13. D. Volm, K. Oettinger, T. Streibl, D. Kovalev, M. Ben-Chorin, J. Diener, B. K. Meyer, J. Majewski, L. Eckey, A. Hoffmann, H. Amano, I. Akasaki, K. Hiramatsu, and T. Detchprohm, Phys. Rev. B **53**, 16543 (1996).

14. M. Tchounkeu, O. Briot, B. Gil, J. P. Alexis, and R.-L. Aulombard, J. Appl. Phys. **80**, 5352 (1996).

CHAPTER 4

OPTICAL TRANSITIONS IN CUBIC GAN

This chapter presents the fundamental optical transitions in cubic GaN and their temperature dependences by cathodoluminescence. Excitonic transitions, donor-acceptor pair (DAP) recombination and its phonon replica are well resolved. By using the thermal activated model, we found that the activation energies of the excitonic and donor-acceptor pair emissions are about 12 meV and 9 meV, respectively. And for temperature below 100 K, the excitonic emission is mainly due to bound excitons . They thermally dissociate into free excitons at higher temperature and vary with temperature as the band gap. The binding energy of the impurities coincides with the thermal activation energy. The donor-acceptor pair was also dissociated into band-acceptor transition with an ionization energy of acceptors around 80 meV. These observations indicate that the ionization energies for both acceptors and donors are smaller than their counterparts in wurtzite structure, which can contribute to efficient doping.*

(*) Part of the results in this chapter is published as "*Free carrier accumulation at cubic AlGaN/GaN heterojunctions"*, Q. Y. Wei, T. Li, J. Y. Huang, F. A. Ponce, E. Tschumak, A. Zado, and D .J. As, Applied Physics Letter, 3 April 2012, Vol. **100**, 142108.

4.1 INTRODUCTION

Since the first report on optical properties of GaN, numerous investigations have been made because of its promising optoelectronic applications.[1] Free exciton emission, donor and acceptor bound exciton emissions, shallow donor-acceptor pair recombination, and the deep yellow band emission have been reported.[1-5] The information obtained can be used to quantify and verify important parameters of GaN, such as free-exciton binding energies, localization energies of excitons bound to impurities, electron and hole effective masses.

The group-III nitrides are naturally stable in the hexagonal wurtzite structure, but recently rapid advances have been achieved in depositing high-quality GaN in the cubic form.[6-9] The absence of polarization effect is one of the advantage of cubic nitrides over the hexagonal counterparts. The cubic GaN can also offer advantage in technological application, in particular, easy cleavage. However, the studies on cubic GaN have been sparse compared with hexagonal GaN, and many basic properties have not been established. This work will investigate the optical properties of cubic GaN and identified the basic emissions based on the temperature dependence of the emission characteristics using cathodoluminescence. In order to fully understand the characteristics of cubic GaN, backgrounds of fundamental emissions are briefly introduced in the following section.

4.2 FUNDAMENTAL EMISSIONS

Excitons are primary candidates for optical assessment of crystal quality. They can be considered in terms of a following model: an electron orbit about a hole due to a coulomb attraction between these two opposite charges. This situation is very similar with the case of a hydrogen atom. So the ionization energy of such a system can be expressed as:

$$\mathrm{E}_x = \frac{-m_r^* q^4}{2h^2\varepsilon^2}\frac{1}{n^2} \qquad (4.1)$$

where n is an integer indicating the exciton states, ε is the dielectric constant of the material, and m_r^* is the reduced mass:

$$\frac{1}{m_r^*} = \frac{1}{m_e^*} + \frac{1}{m_h^*} \tag{4.2}$$

m_e^* and m_h^* being the electron and hole effective masses, respectively.

The electrons and holes which pair off into exctions can recombine, and emit a narrow spectral line, which is called free exciton. In a direct band gap semiconductor with band gap E_g, the energy of the emitted photon is simply

$$h\upsilon = E_g - E_x \tag{4.3}$$

At a cost of lower transition probability, a direct transition can also occur with the emission of one or more optical phonons, called phonon replica with photon energy:

$$h\upsilon = E_g - E_x - mE_p \tag{4.4}$$

where E_p is the phonon energy and m is the number of optical phonons emitted per transition.

In addition to free exciton, a free hole can combine with a neutral donor to form a positively charged excitonic ion, and the electron bound to this donor still travels in a wider orbit about the donor. This complex is called a "donor bound exciton". Similarly, an electron associated with a neutral acceptor is called a "acceptor bound exciton". When they recombine, the emission is characterized by a narrow spectral width at a lower photon energy than that of the free exciton, by an amount of binding energy of the donor or acceptor.

Donors and acceptors can also form pairs and act as stationary molecules embedded in the crystal. The coulomb interaction between a donor and an acceptor results in a lower of binding energies, and the energy separating the paired donor and acceptor states can be written as

$$h\nu = E_g - E_A - E_D + \frac{q^2}{\varepsilon r} \tag{4.5}$$

where E_A and E_D are the binding energies for the donor and acceptor; the fourth term on the right represents the coulomb interaction. Since the impurities are located at discrete sites in the lattice, the distance r varies by finite increments. Thus the interaction between donor and acceptor provides a possible set of states, the emission spectrum should exhibit a fine structure with discrete emission lines. However, at large values of *r*, these emission lines overlap, forming a broad spectrum.

Transitions can also occur between the conduction band and an acceptor state, which produces an emission energy at $h\upsilon = E_g - E_A$, or between a donor state and the valence band, which produces an emission energy at $h\upsilon = E_g - E_D$. In most direct band gap materials, the electron effective mass is considerably smaller than the hole effective mass. Therefore, the binding energy of the donor is smaller than that of the acceptor. Hence, the donor-to-valence-band transition gives higher emission energy than that of the conduction-band-to-acceptor transition. And these two transitions most likely happen in semiconductors with a relatively low concentration of impurities.

4.3 EXPERIMENTAL DETAILS

A cubic $Al_{0.3}Ga_{0.7}N$/GaN heterostructure was grown by plasma assisted molecular beam epitaxy (MBE) on 3C-SiC (001) substrate by Dr. Donat As's group at Paderborn University in Germany.[10] Growth of metastable cubic phase is unfavorable under the equilibrium condition used in metal organic chemical vapor deposition, so MBE technique at lower growth temperature is preferred. The layer thicknesses for GaN and AlGaN are 600 nm and 30 nm, respectively.

Electron holography measurement and simulation of electronic band diagram show that the cubic $Al_{0.3}Ga_{0.7}N$/GaN heterojunction has a quasi two-dimensional electron gas with a density of $5.1\times10^{11}/cm^2$, which originates from the donor states with density of $2\times10^{18}/cm^3$ in the AlGaN layer.[11]

Cathodoluminescence (CL) was performed in a scanning electron microscope operated at an electron acceleration voltage of 5 kV with a beam current of 400 pA. The spectra were obtained from liquid helium temperature up to room temperature.

4.4 OPTICAL CHARACTERIZATION

Figure 4.1 shows the CL spectrum of the cubic $Al_{0.3}Ga_{0.7}N$/GaN heterostructure taken at liquid helium temperature (4 K). Three well-resolved peaks located at 3.29, 3.17 and 3.09 eV, with full-width-at-half-maximums (FWHM) of 33, 38, and 91 meV, respectively, correspond to GaN band-edge emissions. The 3.29 eV peak is assigned to an excitonic transition in cubic GaN, while the 3.17 eV and 3.09 eV peaks are assigned to a donor-acceptor pair (DAP) recombination and its phonon replica, in good agreement with other reports.[12-15] The AlGaN peak is at 3.95 eV with a FWHM of 176 meV, and can be fitted by three Gaussian curves. These peaks are not as well resolved as the GaN band-edge peaks, probably due to alloy fluctuations and residual oxygen contamination. The peak at 3.95 eV gives a range of band gap difference between cubic AlGaN and GaN from 0.66 to 0.78 eV, consistent with the nominal composition of the AlGaN film.

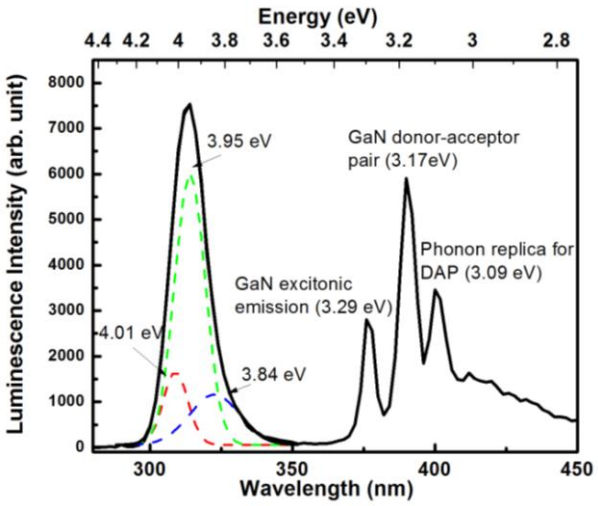

Fig. 4.1. The CL spectrum of the cubic $Al_{0.3}Ga_{0.7}N$/GaN heterostructure taken at liquid helium temperature (4 K). The GaN band-edge emissions (excitonic emission at 3.29 eV and donor-acceptor recombination at 3.17 eV with its phonon replica), and the AlGaN band-edge emission around 3.95 eV are observed.

Figure 4.2 shows the GaN band-edge emissions recorded at different locations at liquid helium temperature. All spectra exhibit the excitonic emission, donor-acceptor recombination and its phonon replica at almost identical positions, but the intensity ratios between these peaks vary sensitively with locations. This spatial inhomogeneity can indicate the defects or impurities forming the donor-acceptor pairs are not homogeneously distributed in the cubic material. Secondary ion mass spectroscopy measurements indicated that oxygen may be the origin of the donor states.[15] We also observed a small peak at 3.43 eV in the top spectrum, which can be an indication of existence of hexagonal phase. At the meantime, the cubic excitonic emission is much reduced, compared with the donor-acceptor pair recombination. These observation may imply that the hexagonal phase exists in the highly defective region, where there is no significant cubic excitonic emission. The presence of hexagonal phase has always been a serious problem due to the metastable nature of cubic phase. However, in this case, we can safely conclude the negligible influence of hexagonal phase based on the very low intensity of the 3.43 eV peak and the absence of this peak from most regions.

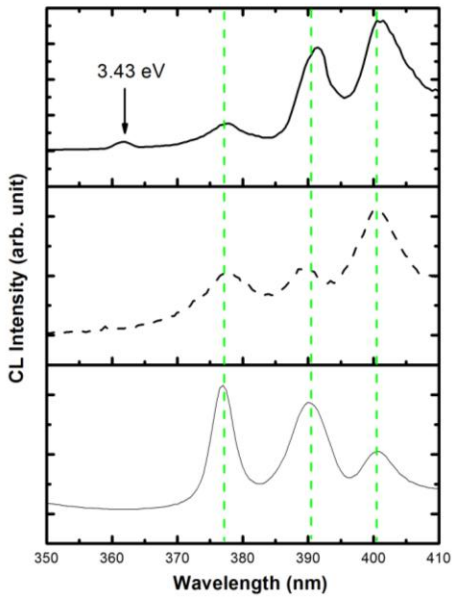

Fig. 4.2. The GaN band-edge emissions recorded at different locations at liquid helium temperature. The three GaN band-edge emissions are observed at almost same positions but with

various intensity ratios. The 3.43 eV peak marked in the top spectrum is originated from hexagonal phase.

The temperature dependence of the GaN band-edge emissions in the range of 4 K- 300 K is depicted in Fig. 4.3. The energy shifts and the intensity variation with temperature can offer more information concerning the nature of the excitonic emission and the binding energy of the impurities. The excitonic emission and the donor-acceptor pair behave in a different way with increasing temperature. The excitonic emission red shifts with temperature, while the donor-acceptor pair recombination blue shifts. The details of intensity variation and energy shifts are demonstrated in Fig. 4.4 and 4.5, respectively.

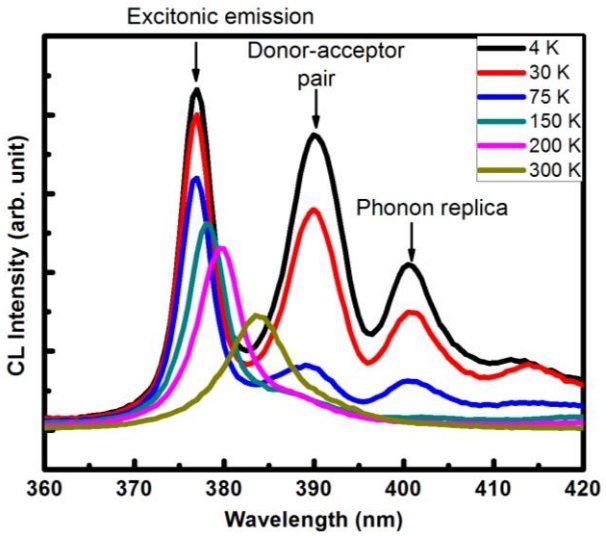

Fig. 4.3. The temperature dependence of the GaN band-edge emission. The excitonic emission red shifts with increasing temperature, while the donor-acceptor pair recombination blue shifts.

In Fig. 4.4 the intensities of excitonic emission (solid triangles) and donor-acceptor pair (solid circles) are plotted vs 1000/T. They both follow the thermal activation model which assumes a thermal activated process is responsible for the reduction of emission intensity and it is described by:

$$I(T) = \frac{I_0}{1 + C\exp(-E_{act}/k_B T)} \tag{4.6}$$

where $I(T)$ is the integrated intensity at temperature T, I_0 and C are constants, k_B is the Boltzmann's constant, and E_{act} is the activation energy. By fitting the experimental data using Eq. (4.6), the activation energies of the excitonic and donor-acceptor pair emissions are found to be about 12 meV and 9 meV, respectively.

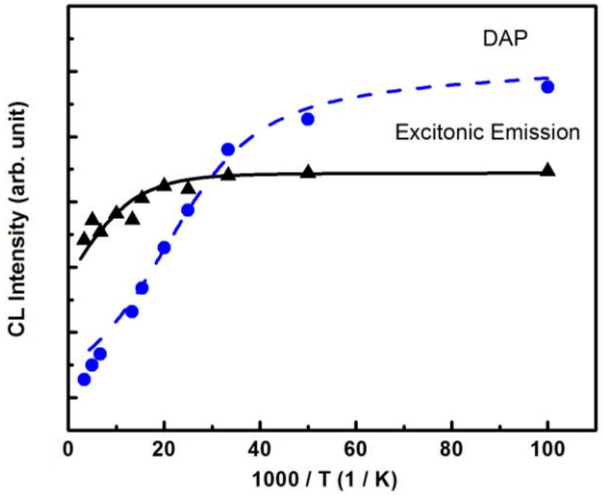

Fig. 4.4. Arrhenius plot of the integrated intensity of the excitonic emission (solid triangles) and the donor-acceptor pair emission (solid circles) vs 1000/T. The curves are calculated assuming a thermal activated process for the reduction of intensity with increasing temperature using Eq. (4.6).

The temperature dependence of the peak energies for excitonic emission and donor-acceptor pair are plotted in Fig. 4.5. At temperature above 100 K, the peak position of the excitonic emission follows the variation of the band gap described by Varshini's equation:

$$E_g = E_0 - \alpha T^2/(T+\beta) \qquad (4.7)$$

where E_0 is the energy gap at 0 K, and α and β are constants. The solid curve in Fig. 4.5 is calculated using Eq. (4.7) and parameters E_0 = 3.302 *eV*, $\alpha = 6.697\times10^{-4}\text{eV}/K$, and $\beta = 600K$.[13] There is a 13 meV deviation at low temperatures which is consistent with the activation energy obtained from the temperature dependence of the intensity. This deviation between 4 K and 100 K, and the excellent agreement with band gap above 100 K indicate that for low temperatures, the excitonic emission is mainly due to bound excitons (BX). Then they

thermally dissociate into free excitons (FX) which dominate at higher temperature and vary with temperature as the band gap. The activation energy is attributed to the ionization energy of the donor which the excitons are bound to. For the donor-acceptor pair, the peak energy increases with temperature up to 100 K. However, the peak energy starts to decrease above 100 K with temperature and follows the trend of the band gap. This can be explained by the transformation from DAP to the conduction-band-to-acceptor transition. The energy difference between the band-acceptor transition (~ 80 meV) is the ionization energy of acceptors.

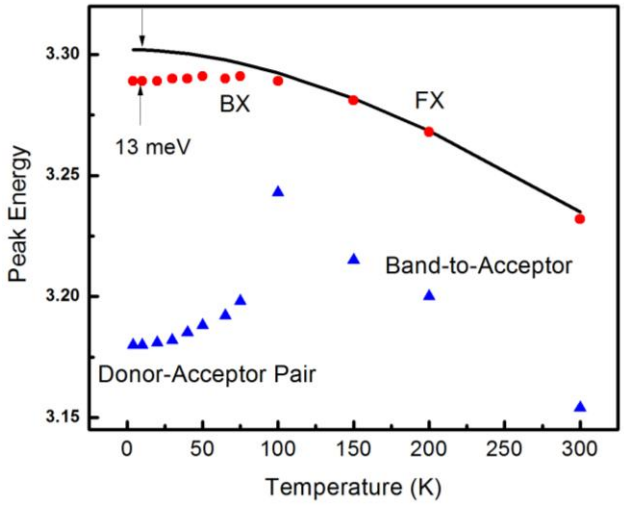

Fig. 4.5. The temperature dependence of the cubic GaN band-edge emissions. Full circles represent the excitonic emission, and triangles represent the DAP and band-acceptor transition. The curve represents the band gap calculated using Eq. (4.7) and parameters in Ref. 13.

4.5 CONCLUSION

The excitonic emission and donor-acceptor recombination with its phonon replica are identified for cubic GaN. The variations of peak intensity and energy with temperature for these emissions are examined. By using the thermal activated model, we found that the activation energies of the excitonic and donor-acceptor pair emissions are about 12 meV and 9 meV, respectively. For temperature below 100 K, the excitonic emission is mainly due to bound excitons . They thermally dissociate into free excitons at higher temperature and vary with temperature as the band gap. The binding energy of the impurities coincides with the thermal

activation energy, and oxygen may be the origin of the donor states. The donor-acceptor pair was also dissociated into the conduction-band-to-acceptor transition with an ionization energy of acceptors around 80 meV. The spatial inhomogeneity of luminescence indicates that defects or impurities forming the donor-acceptor pairs are not uniformly distributed in this material. However, the ionization energies for both acceptors and donors are smller than their counterparts in wurtzite structure, which can contribute to more efficient doping.

REFERENCES

1. R. Dingle, D. D. Sell, S. E. Stokowski, and M. Ilegems, Phys. Rev. B **4**, 1211 (1971).

2. B. Monemar, Phys. Rev. B **10**, 676 (1974).

3. W. Shan, T. J. Schmidt, X. H. Yang, S. J. Hwang, and J. J. Song, Appl. Phys. Lett. **66**, 985 (1995).

4. B. Gil, O. Briot, and R.-L. Aulombard, Phys. Rev. B **52**, R 17028 (1995).

5. C. Merz, M. Kunzer, U. Kaufmann, I. Akasaki, and H. Amano, Semicond. Sci. Technol. **11**, 712 (1996).

6. S. Strite, J. Ruan, Z. Li, A. Salvador, H. Chen, D. J. Smith, W. J. Choyke, and H. Morkoc, J. Vac. Sci. Technol. B **9**, 1924 (1991).

7. S. Miyoshi, K. Onabe, N. Ohkouchi, H. Yaguchi, R. Ito, S. Fukatsu, and Y.Shiraki, J. Cryst. Grow. **124**, 439 (1992).

8. D. Schikora, M. Hankeln, D. J. As, K. Lischka, T. Litz, A. Wagg, T. Buhrowand F. Henneberger, Phys. Rev. B **54**, R8381 (1996).

9. H. Okumura, K. Ohta, G. Feuillet, K. Balakrishnan, S. Chichibu, H. Hamaguchi, P. Hacke, and S. Yoshida, J. Cryst. Grow. **178**, 113 (1997).

10. D. J. As, S. Potthast, J. Schörmann, S. F. Li, K. Lischka, H. Nagasawa, and M. Abe, Materials Science Forum, **527-529**, 1489 (2002).

11. Q. Y. Wei, T. Li, J. Y. Huang, F. A. Ponce, E. Tschumak, A. Zado, and D. J. As, Appl. Phys. Lett. **100**, 142108 (2012).

12. D. J. As, F. Schmilgus, C. Wang, B. Schöttker, D. Schikora, and K. Lischka, Appl. Phys. Lett. **70**, 1311 (1997).

13. G. Ramirez-Flores, H. Navarro-Contreras, A. Lastras-Martinez, R. C. Powell, and J. E. Greene, Phys. Rev. B **50**, 8433 (1994).

14. J. Menniger, U. Jahn, O. Brandt, H. Yang, and K. Ploog, Phys. Rev. B **53**, 1881 (1996).

15. A. Zado, E. Tschumak, K. Lischka, and D. J. As, Semicond. Sci. Technol. **27**, 035020 (2012).

CHAPTER 5

CARRIER LOCALIZATION AND NON-RADIATIVE RECOMBINATION IN INGAN QUANTUM WELLS EMITTING IN THE BLUE, GREEN, AND YELLOW SPECTRAL REGIONS

InGaN quantum wells (QW), with luminescence in the blue, green, and yellow regions of the visible spectrum have been studied by transmission electron microscope (TEM), and conventional and time-resolved cathodoluminescence (CL). TEM results show that compositional inhomogeneties in the well get more significant with increasing emission wavelength. Carrier localization associated with these inhomogeneties in the QWs emitting in the blue and green spectral regions is evidenced by a blueshift in the emission energy with temperature, and a constant radiative lifetime under 50 K for the green-emitting QWs. We also observe the absence of strong localization effects and a relatively high internal quantum efficiency of ~ 12 % for the yellow emitting QWs. On the other hand, the effect of non-radiative recombination on luminescence efficiency also varies with the emission wavelength. The fast increase of the non-radiative recombination rate with temperature in the green emitting QWs contributes to the lower efficiency compared with the blue emitting QWs. The possible saturation of non-radiative recombination above 100 K may explain the unexpected high emission efficiency for the yellow emitting QWs.*

(*) Part of results in this chapter has been published as "*Carrier localization and nonradiative recombination in yellow emitting InGaN quantum wells*", T. Li, A. M. Fischer, Q. Y. Wei, F. A. Ponce, T. Detchprohm, C. Wetzel., Appl. Phys. Lett. **96**, 031906 (2010). Selected to Virtual Journal of Ultrafast Science, 9(2).

5.1 INTRODUCTION

InGaN based quantum well (QW) structures are now widely used in light emitting diodes (LEDs) and laser diodes (LDs) emitting in the blue-green wavelength range.[1] The current luminous efficiency of the GaN-based LED is ~ 100-200 lm/W, which is one order of magnitude higher than standard incandescent light bulbs. Further improvement of light emission efficiency needs careful examination of carrier localization associated with composition inhomogeneities,[2,3] internal electrostatic polarization fields,[4,5] and non-radiative recombination centers [6,7] .

Carrier localization associated with composition fluctuations prevents the diffusion of carriers to non-radiative recombination centers, and it is believed to be responsible for the high light emission efficiency in InGaN-based structures in the violet-blue region. Generally, carriers can be considered localized as long as their spatial extent is much smaller than the typical photon wavelength. For example, monochromatic cathodoluminescence images of InGaN QWs with peak emission at 410 nm have revealed spatially distributed localization centers with dimensions less than 60 nm.[8] Such localization centers are currently related to indium-rich regions that behave as quantum dots.

In this study, we report on the effects of carrier localization and of non-radiative recombination rates on the optical properties of InGaN QWs emitting in the blue, green, and yellow regions of the visible spectrum. Carrier localization is evidenced by a blueshift with temperature in the emission energy, and a relatively constant radiative lifetime for temperatures under 50 K for green-emitting QWs. The absence of strong localization effects is also observed in yellow emitting QWs. The effect of non-radiative recombination on luminescence efficiency also varies with the emission wavelength. We observe a fast increase of the non-radiative rate with temperature in the green emitting QWs, and possible saturation above 100 K in the yellow emitting QWs.

5.2 EXPERIMENT DETAILS

The InGaN/GaN QW structures emitting in the blue, green, and yellow spectral regions were grown by metalorganic vapor phase epitaxy. The structural and optical properties of yellow-emitting InGaN QWs have been recently reported.[9] Five InGaN QWs were grown with a thickness of ~ 3 nm, separated by GaN barriers ~200 nm thick. The QW structure was then capped with a GaN layer ~ 200 nm thick. The microstructure of the InGaN QWs was studied by transmission electron microscopy (TEM) operating at 200 kV. The TEM specimens were prepared by mechanical wedge-polishing techniques, followed by ion milling in a cold stage in order to minimize indium diffusion. The optical properties were studied by cathodoluminescence (CL) in a scanning electron microscope. CL spectra were obtained for temperatures ranging from liquid-helium to room temperature, with an electron acceleration voltage of 5 kV and a beam current of 400 pA. Time-resolved CL (TRCL) was performed with a 100 ns electron pulse width at a 1 MHz repetition rate. The pulse rise and fall times were below 100 ps with an overall system resolution under 400 ps measured with a GaAs photocathode detector.

5.3 MICROSTRUCTURAL PROPERTIES

Figure 5.1 shows cross-section TEM images of InGaN QWs emitting in the green spectral region. The interfaces between wells and barriers appear sharp, and with no variations in the thickness. There is a slight contrast variation in the well layers with spherical shape of 3-5 nm in size, as shown in Fig. 5.1(b) and (c), which indicates small compositional fluctuations. The microstructure of the yellow emitting InGaN QWs is shown in Fig. 5.2. The contrast in the well layers is more inhomogeneous than that of the green InGaN QWs, with islands of lateral dimensions between 15 and 30 nm, as seen in Fig. 5.2(b). We observe a dark line in the middle of the wells in Fig. 5.2(b) with fading contrast towards the GaN barriers. Small clusters with 2 to 3 nm in size are observed in the high-resolution TEM image of Fig.5.2(c). The clusters that are well oriented along the projection exhibit a spherical shape. Considering that the TEM image is a

2-dimensional projection along the $[11\bar{2}0]$ projection, the spatial distribution of the indium cluster units along the zone axis may result in this symmetric contrast since the clusters are much smaller than the specimen thickness (~ 100 nm). Limitations in the TEM sample preparation and possible instability of very thin InGaN samples prevent us from making a stronger statement about the nature of these clusters. However, it is clear that the indium composition inhomogeneities in the well layer become more significant with increasing indium composition.

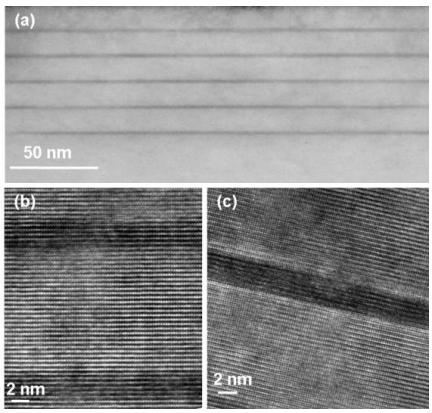

Fig. 5.1. Transmission electron microscopy images of green-emitting InGaN/GaN QWs. (a) Bright field image with g= (0002). (b) High resolution image of bottom two QWs and (c) High resolution image of top QW.

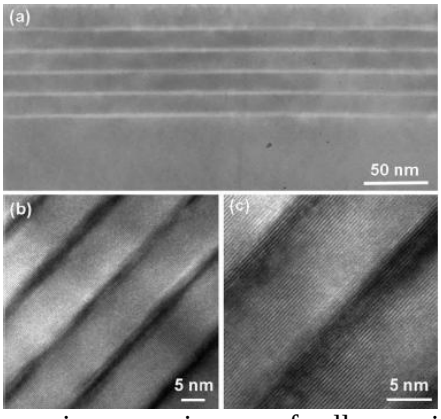

Fig. 5.2. Transmission electron microscopy images of yellow-emitting InGaN/GaN QWs. (a) Dark field image with g= (0002). (b) High resolution image of all five QWs and (c) High resolution image of top two QWs.

5.4 OPTICAL PROPERTIES

The variation of the blue emitting QW emission spectra in the temperature range from 5 to 300K is shown in Fig. 5.3(a). The emission peaks in the spectra fit well with a single Gaussian

function. A main emission centered at 448 nm with a full width at half maximum (FWHM) of 17 nm is observed at room temperature. The peak energies versus temperature are plotted in Fig.5.3(b). An S-shape temperature dependence of the QW peak emission energy is observed, and this behavior has already been reported for both InGaN and AlGaN material systems.[10-13] It is characterized by an initial red-shift with temperature ($T<T_1$) followed by a blue-shift ($T_1<T<T_2$) and finally another red-shift at higher temperatures ($T>T_2$). The characteristic temperatures T_1 and T_2 vary significantly for QWs emitting in different spectral regions. For the blue emitting QW structure in Fig. 5.3(b), T_1 is 100 K and T_2 is 200 K. Such energy shifts with temperature can be explained using an exciton relaxation and thermalization models.[13] While excitons may be immobile at very low temperatures, they are able to overcome the potential fluctuations and relax into lower potential minima with increasing temperatures ($T < T_1$). This becomes evident by a red-shift in the emission peak. Thermalization of excitons out of potential minima may occur at higher temperatures ($T_1 < T < T_2$), which results in a blue-shift of the emission peak. At even higher temperatures ($T > T_2$), a decreasing band gap energy due to lattice expansion results in the final red-shift of the emission energy. The intermediate blue-shift in the S-shaped behavior is perceived evidence of the presence of localized states. The temperature range ($T_1 < T < T_2$) reflects the degree of potential energy fluctuations.

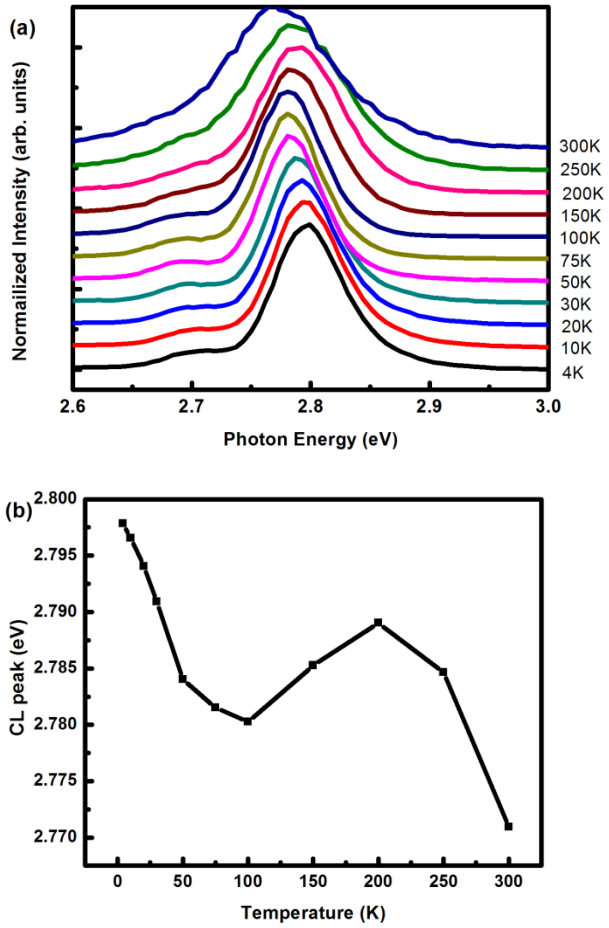

Fig. 5.3. Cathodoluminescence of the blue QWs measured in the temperature range from 5K to 300K. (a) Normalized spectra taken at temperatures specified on the right. (b) Plot of the QW emission peak energy vs temperature. The peak energy values were obtained by fitting with Gaussian functions.

Figures 5.4 and 5.5 show the variation of emission spectra in the same temperature range for the InGaN QWs emitting in the green and yellow spectra regions, respectively. The QWs in Fig. 5.4 emit at 514 nm with a FWHM of 31 nm at room temperature, while the ones in Fig. 5.5 emit at 578 nm with a FWHM of 51 nm. It is apparent that the FWHM of the QW emission peak increases with emission wavelength. This can be explained by compositional disorder or poorer interface quality. For the green emitting QWs in Fig. 5.4(b), a similar *S*-shaped temperature dependence of the peak energy is observed. A blue-shift is observed from 50 K to 200 K, this being a wider temperature range than in the case of blue emitting QWs (that range from 100 K to

200 K). The behavior is different for the yellow emitting QWs in Fig. 5.5(b), where the peak energy is seen to decrease monotonically with temperature. No blue shift associated with a transition from localized states into extended states is observed, indicating an absence of carrier localization in yellow emitting InGaN QWs.

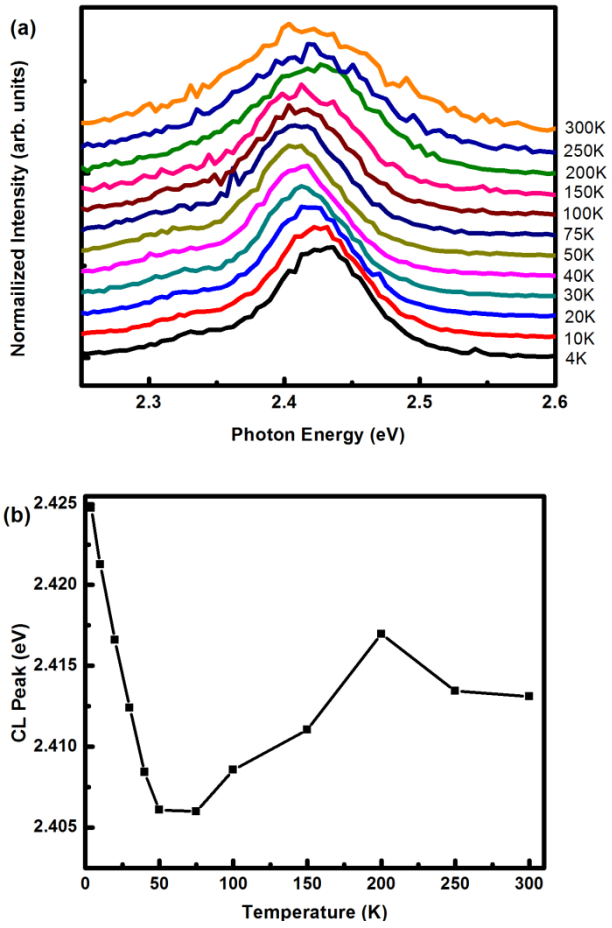

Fig. 5.4. Cathodoluminescence of the green QWs measured in the temperature range from 5K to 300K. (a) Normalized spectra taken at temperatures specified on the right. (b) Plot of the QW emission peak energy vs temperature.

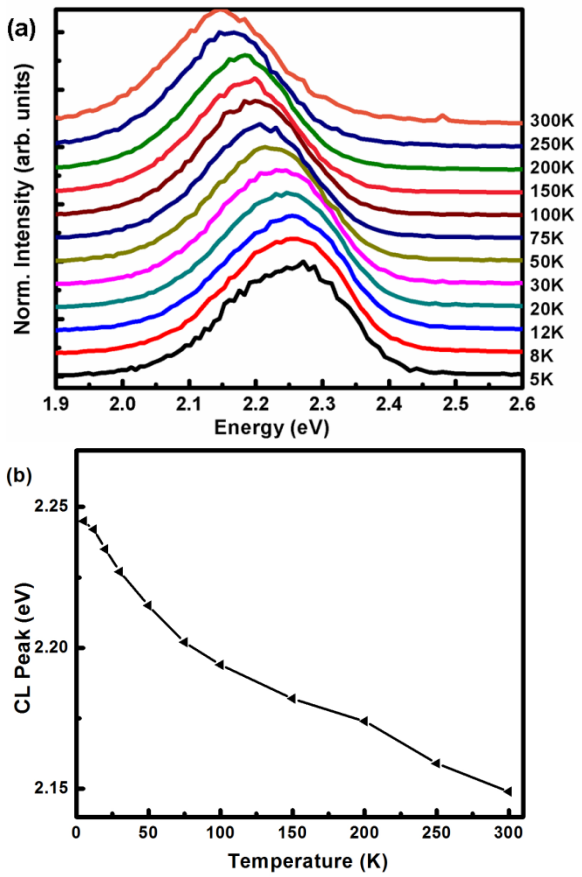

Fig. 5.5. Cathodoluminescence of the yellow QWs measured in the temperature range from 5K to 300K. (a) Normalized spectra taken at temperatures specified on the right. (b) Plot of the QW emission peak energy vs temperature.

In order to further understand the carrier dynamics in the InGaN QWs, time-resolved CL was performed as a function of temperature. Figure 5.6(a) shows luminescence transients for the peak emission of the blue emitting QWs taken at temperatures of 5, 100, and 300K. At all these temperatures, the luminescence initially decays at an almost constant rate, with a lifetime of ~ 15 ns. The CL lifetimes were obtained by fitting the luminescence transients (choosing the time interval from the maximum intensity to 1/100 of the maximum to avoid background noise) with an exponential function. This indicates that non-radiative recombination centers are suppressed, even with increasing temperature. The temperature dependence of the CL lifetime (τ), the radiative lifetime (τ_R), and the non-radiative lifetime (τ_{NR}) is shown in Fig. 5.6(b). Under the assumption that radiative recombination is dominant at sufficiently low temperature, an upper

value of the internal quantum efficiency (η) at different temperature can be determined.[14, 15] The radiative and non-radiative lifetimes were derived on the basis of the following equations:

$$\eta = (\frac{1}{\tau_R}) / (\frac{1}{\tau}) \qquad (5.1)$$

$$\frac{1}{\tau} = \frac{1}{\tau_R} + \frac{1}{\tau_{NR}} \qquad (5.2)$$

There is slight variation of non-radiative lifetime above 25 K, which may be due to the suppression of non-radiative centers. On the other hand, the radiative lifetime increases linearly with temperature up to 150 K. The temperature dependence of the radiative lifetime provides a direct measure of the excitonic dimensionality. Excitons confined in a zero-dimensional potential (e. g. a quantum dot) exhibit a constant radiative lifetime with temperature. For excitons in two-dimensional extended states, the radiative lifetime increases linearly with temperature.[16, 17] The linear behavior of radiative lifetimes in the blue InGaN QWs between 25 and 150 K indicates a two-dimensional exciton recombination nature.

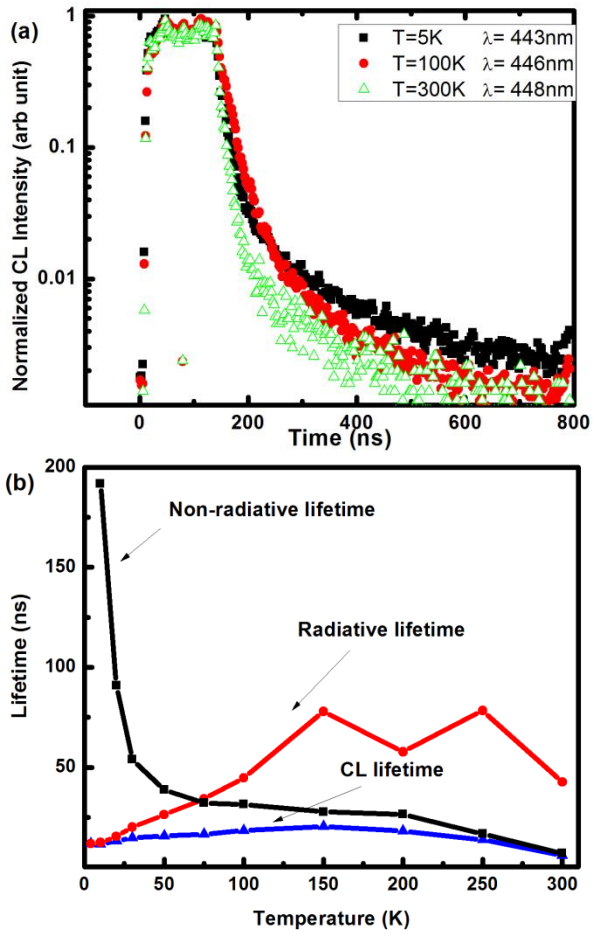

Fig. 5.6. Time-resolved cathodoluminescence of the blue QWs. (a) Transients for the peak emission energy at 5K, 100K and 300K. (b) Plot of the CL lifetime, the radiative lifetime, and the non-radiative lifetime across the temperature range.

Figures 5.7 and 5.8 show the luminescence transients and recombination lifetimes for the green and yellow emitting QWs. The green emitting QWs exhibit a constant CL lifetime of ~ 100 ns up to 100 K, which is much longer than the lifetime of the blue emitting QWs (~ 15 ns). This can be understood by the effect of an increase in the piezoelectric field and degradation of the material quality with indium composition. In addition, a much faster decay in luminescence with lifetime of ~ 38 ns is observed at room temperature. This can be explained as follows: luminescence decay is the result of competition between radiative and non-radiative recombinations. At room temperature, non-radiative recombinations are much faster than radiative recombinations. This is the reason why we observe much faster luminescence decay at

room temperature. On the other hand, the yellow emitting QWs in Fig. 5.8 show the fastest decay at low temperature, probably dominated by radiative processes. As temperature reaches 100 K, the decay becomes significantly slower. However, at temperatures above 100 K, the CL decay remains almost independent of temperature. This may indicate that the non-radiative recombination saturates at such temperatures. The dependence of the radiative lifetime with temperature is also different between the green and yellow emitting QWs. The radiative lifetime remains almost constant below 50 K for the green emitting QWs, which indicates localization of excitons in quantum-dot-like structures. This finding is consistent with the blue-shift we observed in emission energy, and evidences the existence of localization centers. For the yellow QWs, the radiative lifetime increases proportionally to temperature up to ~ 100 K. There is no temperature range where the radiative lifetime remains constant, which is further support of exciton localization not playing a major role in this material. The absence of localization effects is in line with earlier reports on high-power green LEDs.[18]

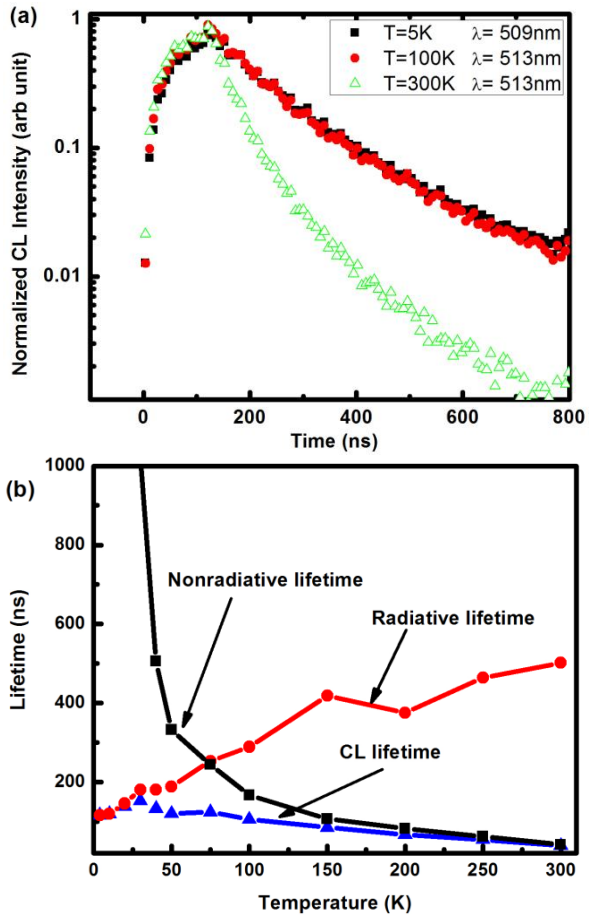

Fig. 5.7. Time-resolved cathodoluminescence of the green QWs. (a) Transients for the peak emission energy at 5K, 100K and 300K. (b) Plot of the CL lifetime, the radiative lifetime, and the non-radiative lifetime across the temperature range.

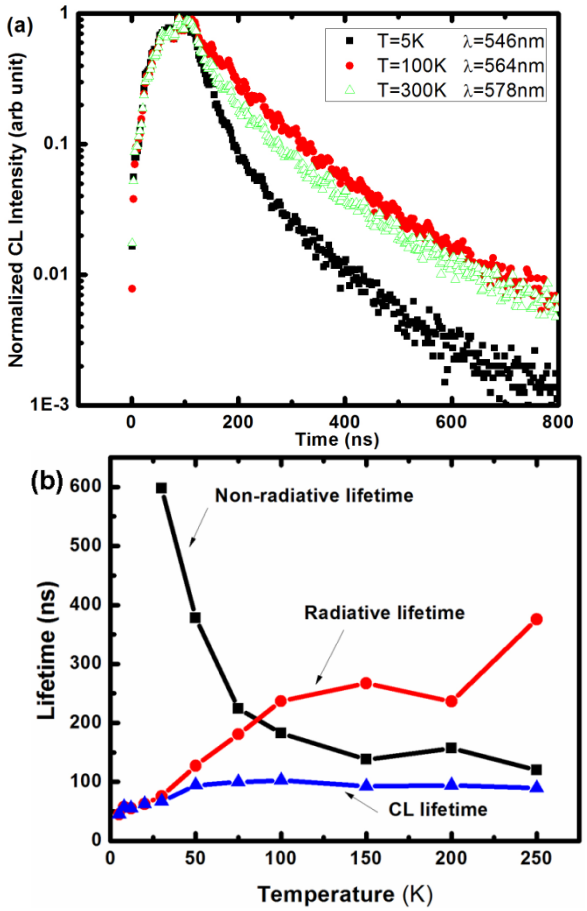

Fig. 5.8. Time-resolved cathodoluminescence of the yellow QWs. (a) Transients for the peak emission energy at 5K, 100K and 300K. (b) Plot of the CL lifetime, the radiative lifetime, and the non-radiative lifetime across the temperature range.

To summarize the temperature dependence of peak energy and lifetime, we propose the following schematic band model as shown in Fig. 5.9. In the blue emitting QWs, excitons can be trapped in the shallow potential minima and they can be excited out of the trap when temperature is increased, which results in the observed blueshift. However, the potential minima have relatively larger spatial dimensions than quantum dots, so the radiative lifetime doesn't follow the characteristics of the excitons localized in zero-dimensional potential. With increasing indium composition (i.e. for the green emitting InGaN QWs), the potential fluctuations due to the composition variation become more significant, and localization centers with much deeper energy depth and smaller size appear. These can explain the blueshift which occurs in a wider temperature range and the linear temperature dependence of radiative lifetime. In the QWs with

higher indium content (i.e. the yellow emitting QWs), indium clusters acting as localization centers are no longer far apart. They are close enough so that the localized states in the respective potential minima can interact with each other and form a mini-band. In this case, excitons occupy extended states in the mini-band, and they are not spatially localized anymore. As a result, there is no blueshift related to the transition from localized states to extended states, and the radiative lifetime exhibits a two-dimensional behavior in extended states. This may explain the higher internal quantum efficiency observed for the yellow InGaN QWs.

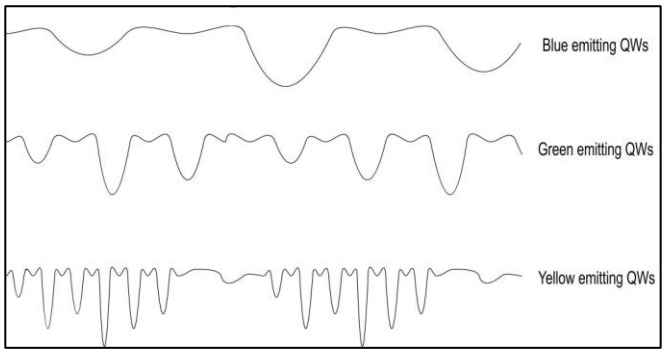

Fig. 5.9. Schematic band model for blue, green and yellow QWs, showing different types of localization.

5.5 SUMMARY

In summary, we have investigated the effects of carrier localization and non-radiative recombination for InGaN/GaN QWs emitting in the blue, green and yellow spectral regions. The carrier localization is investigated by the temperature dependence of the emission energy and radiative lifetime. The extent of localization varies in QWs with increasing emission wavelength. The blue emitting QWs show a blueshift in the emission energy associated with thermalization of carriers out of potential minima, but no indication of localization centers with dimensions similar to quantum-dots. The green emitting QWs are characterized by the *S*-shape temperature dependence of emission energy and an almost constant radiative lifetime below 50 K. Both results indicate carrier localization due to compositional inhomogeneties. For the yellow emitting QWs, we show that the peak energy exhibits no blue-shift, and the temperature dependent TRCL

measurement confirms the absence of pronounced effects due to carrier localization. The formation of miniband due to closely-distributed indium clusters is proposed to explain this phenomenon. On the other hand, the non-radiative recombination also plays different roles in these structures. In the blue emitting QWs, the non-radiative lifetime is almost independent of temperature above 25 K, indicating that it is severely suppressed. The green emitting QWs have a much shorter non-radiative lifetime than the radiative one at room temperature, and it indicates that the non-radiative recombination is the limiting factor of the internal quantum efficiency. For the yellow emitting QWs, the non-radiative recombination is also responsible for the decrease of efficiency with temperature, but the saturation above 100 K may contribute to the high efficiency at room temperature.

REFERENCES

1. F. A. Ponce and D. P. Bour, Nature **386**, 351 (1997).

2. S. Chichibu, T. Azuhata, T. Sota, and S. Nakamura, Appl. Phys. Lett. **69**, 4188 (1996).

3. T. Mukai, M. Yamada, and S. Nakamura, Jpn. J. Appl. Phys. **37**, L1358 (1998).

4. T. Takeuchi, C. Wetzel, S. Yamaguchi, H. Sakai, H. Amano, I. Akasaki, Y. Kaneko, S. Nakagawa, Y. Yamaoka, and N. Yamada, Appl. Phys. Lett. **73**, 1691 (1998).

5. J. Bai, T. Wang, and S. Sakai, J. Appl. Phys. **88**, 4729 (2000).

6. D. Cherns, S. J. Henley, and F. A. Ponce, Appl. Phys. Lett. **78**, 2691 (2001).

7. A. Hangleiter, F. Hitzel, C. Netzel, D. Fuhrmann, U. Rossow, G. Ade, and P. Hinze, Phys. Rev. Lett. **95**, 127402 (2005).

8. S. Chichibu, K. Wada, and S. Nakamura, Appl. Phys. Lett. **71**, 2346 (1997).

9. T. Li, A. M. Fischer, Q. Y. Wei, F. A. Ponce, T. Detchprohm, and C. Wetzel, Appl. Phys. Lett. **96**, 031906 (2010).

10. Y.-H. Cho, G. H. Gainer, A. J. Fischer, J. J. Song, S. Keller, U. K. Mishra, and S. P. DenBaars, Appl. Phys. Lett. **73**, 1370 (1998).

11. H. P. D. Schenk, M. Leroux, and P. de Mierry, J. Appl. Phys. **88**, 1525 (2000).

12. J. Li, K. B. Nam, J. Y. Lin, and H. X. Jiang, Appl. Phys. Lett. **79**, 3245 (2001).

13. A. Bell, S. Srinivasan, C. Plumlee, H. Omiya, F. A. Ponce, J. Christen, S. Tanaka, A. Fujioka, and Y. Nakagawa, J. Appl. Phys. Lett. **95**, 4670 (2004).

14. Y. Narukawa, S. Saijou, Y. Kawakami, Sg. Fujita, T. Mukai, and S. Nakamura, Appl. Phys. Lett. **74**, 558 (1999).

15. R. C. Miller, D. A. Kleinman, W. A. Nordland, Jr., and A. C. Gossard, Phys. Rev. B **22**, 863 (1980).

16. Y. Narukawa, Y. Kawakami, Sg. Fujita, and S. Nakamura, Phys. Rev. B **59**, 10823 (1998).

17. Y. Kawakami, K. Omae, A. Kaneta, K. Okamoto, Y. Narukawa, T. Mukai, and Sg. Fujita, J. Phys.: Condens. Matter **13**, 6993 (2001).

18. C. Wetzel, T. Salagaj, T. Detchprohm, P. Li, and J. S. Nelson, Appl. Phys. Lett. **85**, 866 (2004).

CHAPTER 6

THE EFFECT OF INGAN UNDERLAYERS ON THE ELECTRONIC AND OPTICAL PROPERTIES OF INGAN/GAN QUANTUM WELLS

This chapter presents the effect of InGaN underlayers on the electronic and optical properties of visible InGaN/GaN quantum well structures. A significant improvement of the QW emission efficiency is observed as a result of the insertion of the $In_{0.03}Ga_{0.97}N$ underlayers, which is associated with a blueshift in the emission energy, a reduced recombination lifetime, an increased spatial homogeneity in the QW luminescence, and a weaker internal field across the QWs. These are explained by partial strain relaxation evidenced by reciprocal space mapping of the X-ray diffraction intensity. Electrostatic potential profiles obtained by electron holography provide evidence for enhanced carrier injection by tunneling from the underlayer into the first QW.

6.1 INTRODUCTION

InGaN quantum wells (QWs) are widely being used in blue and green light emitting diodes (LED)and laser diodes (LD), which are characterized by high emission efficiencies and long device lifetime.[1] Further improvements in emission efficiency of these devices are currently limited by various factors, such as compositional fluctuations,[2,3] threading dislocations,[4] and the internal electrostatic fields.[5] The latter consist of spontaneous polarization and strain-induced piezoelectric fields that result in the spatial separation of electrons and holes in the QWs, causing a red shift in the emission energy and an increase in the recombination lifetime.

In conventional LED or LD structures, the InGaN/GaN QWs are sandwiched between p-type and n-type GaN layers acting as waveguides which have higher band gap and lower refraction index. A significant increase in the internal quantum efficiency has been achieved by the introduction of InGaN underlayers prior to the QW growth, which result in reduction of non-radiative recombination centers and improved indium compositional uniformity in the QWs.[6,7] Thick InGaN layers are also employed as waveguides in laser diodes.[8,9] Despite the reported benefits of using InGaN underlayers, their role in the improvement of light emission efficiency still remains unclear.

In this chapter, we report on the electrical and optical properties that lead to an improvement in the emission efficiency of a blue-emitting $In_yGa_{1-y}N$ QW structure grown on an $In_xGa_{1-x}N$ underlayer. The properties have been measured using cathodoluminescence (CL), electron holography (EH), and reciprocal space mapping (RSM) of the X-ray diffraction (XRD) intensity . A strong correlation is found between light emission characteristics, the strain distribution and the internal electrostatic fields. We show that the $In_xGa_{1-x}N$ underlayer mitigates the internal field resulting in a blue shift in emission energy and reduced radiative lifetimes, and improves the compositional uniformity of $In_yGa_{1-y}N$ in the QWs that contributes to a more uniform distribution of luminescence. These finding are due to partial strain relaxation

demonstrated by RSM. Furthermore, electrostatic potential profiles by EH give evidence of enhanced injection of carriers into the active region.

6.2 EXPERIMENTAL DETAILS

The thin film structures reported here were grown by metalorganic chemical vapor deposition using standard techniques.[9] The layer sequence is shown in Table 6.1. A 4-um-thich GaN layer was grown on a sapphire substrate. This was followed by an AlGaN/GaN superlattice (130 pairs, each layer 2.4 nm thick), and a 100-nm-thick GaN layer; these layers were doped with silicon. An 80-nm-thick $In_{0.03}Ga_{0.97}N$ underlayer was then deposited, followed by four 2.8-nm-thick $In_yGa_{1-y}N$ QWs separated by 8.8-nm-thick Si-doped GaN barriers. An 8.8-nm-thick unintentionally doped GaN layer was grown for protection on top of the QWs. This thin capping layer is designed for simultaneous determination of the electronic and optical properties of the QW structure using electron holography and cathodoluminescence. For comparison, a similar QW structure was grown directly on GaN without the InGaN underlayer. These two structures have a target emission wavelength (λ) in the 400-420 nm range.

Table 6.1. *Thin film structure with an InGaN underlayer used in this study*.

Layer	Material	Thickness (nm)	[In] or [Al]
Capping layer	GaN:ud	8.8	
Active region (4 pairs)	InGaN GaN:Si	2.8 8.8	0.10
Underlayer	InGaN:ud GaN:Si	80 100	0.03
Cladding (150 pairs)	GaN:Si AlGaN:Si	2.4 2.4	0.16
GaN layer	GaN:Si GaN:ud	3000 1000	
Substrate	Sapphire		

6.3 CL EMISSION CHARACTERISTICS

Figure 6.1 shows the CL spectra of QW structures with and without an $In_{0.03}Ga_{0.97}N$ underlayer, taken at liquid helium temperatures. Even though the QW structure in both cases was grown under the same conditions, an emission peak at λ~410 nm (3.024 eV) is observed for the thin film structure with the InGaN underlayer, which represents a 10 nm blue shift with respect to the case without the InGaN underlayer that emits at λ ~ 420 nm. This blue shift can be explained by a reduction of electric fields in the QWs by the InGaN underlayer.

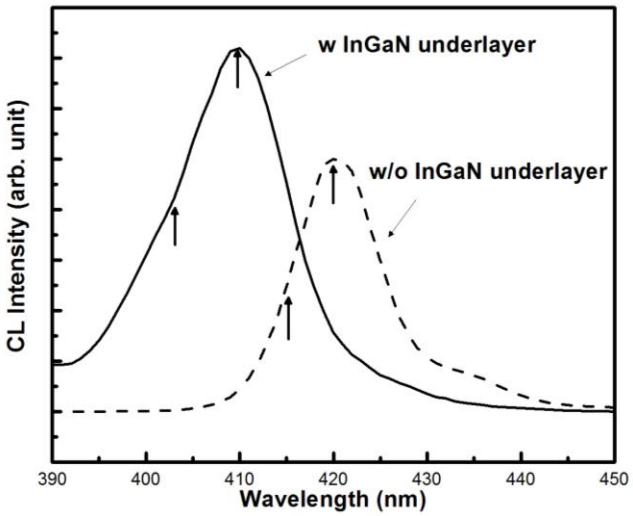

Fig. 6.1. Cathodoluminescence (CL) spectra of the multiple quantum-well (MQW) emission measured at a temperature of 4.5 K with an electron accelerating voltage of 4 kV for layer structures with and without an $In_{0.03}Ga_{0.97}N$ underlayer. Arrows indicate wavelengths at which monochromatic images are shown in Fig. 6.2.

Monochromatic CL images taken at the wavelengths indicated by arrows in Fig. 6.1 are shown in Fig. 6.2. The sample without an InGaN underlayer in Fig. 6.2(a) exhibits a large spatial variation of the QW luminescence, and a complementary contrast is observed between the images taken at the peak (421 nm) and the lower-wavelength shoulder (415 nm) of the QW emission. This complementary contrast indicates inhomogenous distribution of indium composition in the QW plane. The bright and dark contrasts at λ ~ 415 nm in Fig. 6.2(a) can be attributed to indium-poor and indium-rich regions, respectively. The inhomogeneity in indium incorporation in the

QWs may happen due to variations in strain during epitaxy, as first observed in SiGe growth.[10] On the other hand, for the sample with the InGaN underlayer in Fig. 6.2(b), a higher spatial homogeneity in the luminescence is observed. This can be explained by increased uniformity indium incorporation due to lower strain in the QW layers.

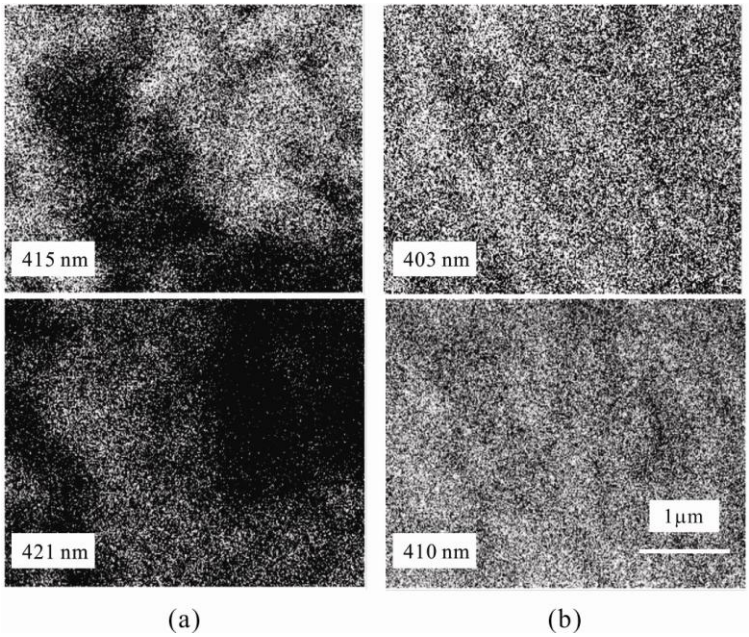

Fig. 6.2. Monochromatic CL images taken at the peak and the lower-wavelength shoulder of the QW emission for the layer structures (a) without and (b) with $In_{0.03}Ga_{0.97}N$ underlayer.

In order to further explore the influence of the InGaN underlayer on the optical properties of the active region, time-resolved CL was performed on both samples. Figure 6.3 shows luminescence transients taken at the QW emission peak, using a pulsed electron beam of 100 ns width at a 100 kHz repetition rate. After the electron beam is switched on at t = 0 ns, the luminescence intensity builds up, eventually reaching a quasi-steady state. At t= 100 ns, the electron beam is switched off and decay in luminescence is observed. The recombination lifetime can be extracted from the transient by fitting the luminescence decay with a single exponential function. The sample with the InGaN underlayer exhibits a much shorter recombination lifetime (10 ns) than the sample without the InGaN underlayer (29 ns). This decrease in lifetime can be

explained by the reduction of the internal field in the QWs which enhances the overlap of electron and hole wave functions, thus increasing the radiative recombination rate.

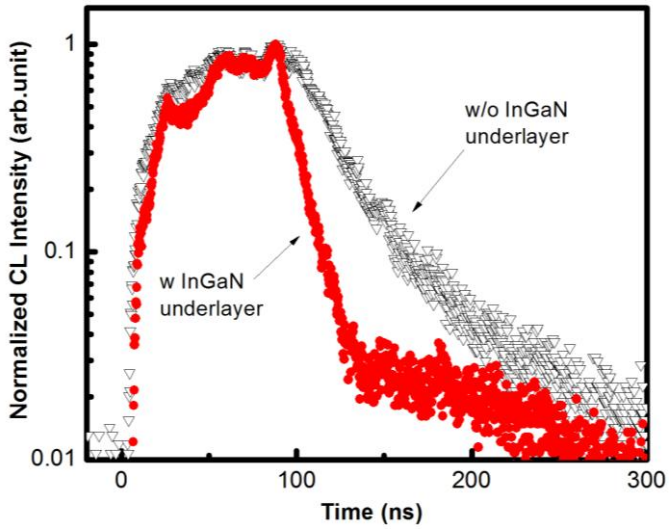

Fig. 6.3. Time-resolved CL transients for the peak energy of the emission for QWs with an $In_{0.03}Ga_{0.97}N$ underlayer (solid circles), and without underlayer (open triangles).

6.4 ENERGY POTENTIAL PROFILE IN THE QW

In order to understand the effect of the InGaN underlayer on the QW emission, we used a transmission electron microscope (TEM) equipped with a biprism for EH measurements to profile the electrostatic potential across the QWs. More experimental details about the technique can be found elsewhere.[11,12] The electrostatic potential energy across the QWs is shown in Fig. 6.4 for layer structures with and without the InGaN underlayer. Due to a limited field of view in EH, only the bottom three QWs are shown. The energy scale of the electrostatic potential profile was calibrated by using the QW emission energies from the CL measurements combined with a self-consistent 1-D Schrödinger simulation. As shown in Fig. 6.4 (a), the electric field in each QW is ~ 0.83 MV/cm and does not vary in the growth sequence. The introduction of an InGaN underlayer results in a non-uniform potential profile along the growth direction, as shown in Fig. 6.4(b). The band offset and the internal field in the second and third QWs have average values of 0.32 eV and 0.66 MV/cm, respectively. This is consistent with the CL observation that the

emission from the sample with the InGaN underlayer has higher emission energy. The first (left) QW shows different characteristics than the other two QWs. The difference can be explained either by a lower indium incorporation in the left QW or, and most likely, due to free-electron tunneling from the InGaN underlayer. The 80-nm-thick InGaN underlayer with a lower band gap than the GaN quantum barrier acts as a reservoir for electrons. These electrons can partially fill the QW reducing the band offset in the first QW. Drift of these electrons and their contribution to the interface charge density produce an additional field opposite to the piezoelectric field, resulting in a weaker electric field in the QW. The accumulation of electrons in the first QW may lead to an enhancement of hole injection into the other QWs which may contribute to their observed higher luminescence intensity and efficiency.

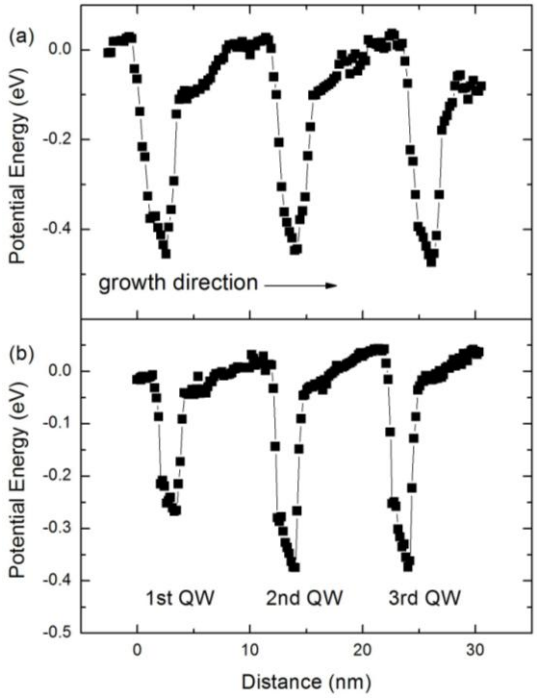

Fig. 6.4. Electrostatic potential across the top QWs determined by electron holography for layer structures (a) without and (b) with $In_{0.03}Ga_{0.97}N$ underlayer.

6.5 STRAIN DISTRIBUTION

The reduction of the electric fields in the QWs for the case with InGaN underlayer can be explained by strain relaxation. The strain in these structures are characterized by reciprocal

spacing mapping (RSM) of the X-ray diffraction (XRD) intensity at the (105) diffraction peak shown in Fig. 6.5. The Q_x and Q_y axes represent the reciprocals of lattice parameters *a* and *c*, respectively, where $Q_x = \lambda/(\sqrt{3}\,a)$, $Q_y = 5\lambda/(2c)$ and λ is the wavelength of the X-ray. In the RSM of the structure without InGaN underlayer in Fig. 6.5(a), the peaks of AlGaN superlattice, GaN, and InGaN QWs align with each other, at Q_x =0.2784. This means that these layers are grown pseudomorphically. For the structure with InGaN underlayer shown in Fig. 6.5(b), the peaks of InGaN underlayer and QW satellite are both shifted to the left, at Q_x = 0.2780. The satellite peak represents the average spacing of the basal planes in the active region, i.e. the QWs and barriers. This shift is explained by a partial relaxation introduced by InGaN underlayer, which accounts for ~4/9 of full relaxation. TEM images (not shown here) also give evidence of misfit dislocation generation at the lower interface of the InGaN underlayer.

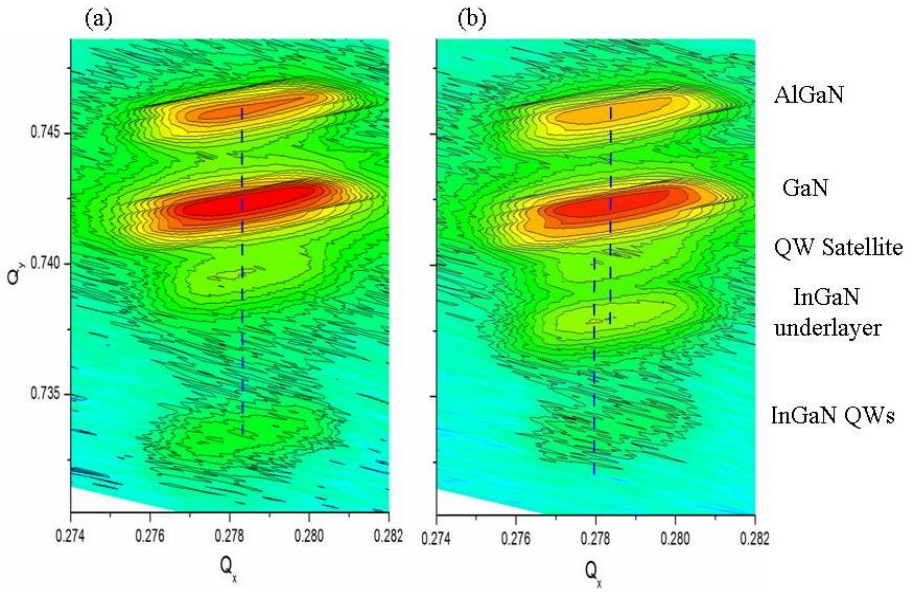

Fig. 6.5. Reciprocal space mapping of the X-ray diffraction intensity around the diffraction spot (105) for layer structures (a) without and (b) with $In_{0.03}Ga_{0.97}N$ underlayer.

6.6 SUMMARY

In conclusion, a blue shift of emission energy and a reduced recombination lifetime due to the reduction of internal fields have been observed when using InGaN underlayers, which is in

part responsible for the improved emission efficiency. Electron holography potential profiles also show an overall reduction of internal fields which is consistent with the optical results. Additionally, in the layer structure with the InGaN underlayer the first QW exhibits a different potential profile than the other QWs, which we interpret to be associated with tunneling of electrons from the underlayer. These characteristics contribute to the reduction of the internal field and the increased luminescence intensity.

REFERENCES

1. F. A. Ponce, S. Srinivasan, A. Bell, L. Geng, R. Liu, M. Stevens, J. Cai, H. Omiya, H. Marui, and S. Tanaka, Phys. Stat. Sol. B **240**, 273 (2003).

2. S. Chichibu, T. Azuhata, T. Sota, and S. Nakamura, Appl. Phys. Lett. **69,** 4188 (1996).

3. S. Srinivasan, F. Bertram, A. Bell, F. A. Ponce, S. Tanaka, H. Omiya, and Y. Nakagawa, Appl. Phys. Lett. **80**, 550 (2002).

4. S. D. Lester, F. A. Ponce, M. G. Craford, and D. A. Steigerwald, Appl. Phys. Lett. **66**, 1249 (1995).

5. T. Takeuchi, C. Wetzel, S. Yamaguchi, H. Sakai, H. Amano, I. Akasaki, Y. Kaneko, S. Nakagawa, Y. Yamaoka, and N. Yamada, Appl. Phys. Lett. **73**, 1691 (1998).

6. T. Akasaka, H. Gotoh, T. Saito, and T. Makimoto, Appl. Phys. Lett. **85**, 3089 (2004).

7. J. K. Son, S. N. Lee, T. Sakong, H. S. Paek, O. Nam, Y. Park, J. S. Hwang, J. Y. Kim, and Y. H. Cho, J. Cryst. Growth **287**, 558 (2006).

8. K. M. Kelchner, Y. D. Lin, M. T. Hardy, C. Y. Huang, P. S. Hsu, R. M. Farrell, D. A. Haeger, H. C. Kuo, F. Wu, K. Fujito, D. A. Cohen, A. Chakraborty, H. Ohta, J. S. Speck, S. Nakamura, and S. P. DenBaars, Appl. Phys. Express **2**, 071003 (2009).

9. J. P. Liu, Y. Zhang, Z. Lochner, S.-S. Kim, H. Kim, J.-H. Ryou, S.-C. Shen, P. D. Yoder, R. D. Dupuis, Q. Y. Wei, K. W. Sun, A. M. Fischer, and F. A. Ponce, J. Cryst. Growth **315**, 272 (2011).

10. A. J. Pidduck, D. J. Robbins, A. G. Cullis, W. Y. Leong, and A. M. Pitt, Thin Solid Films **222**, 78 (1992).

11. J. Cai and F. A. Ponce, J. Appl. Phys. **91**, 9856 (2002).

12. F. A. Ponce, Ann. Phys. (Berlin) **523**, 75 (2011).

CHAPTER 7

SUMMARY AND FUTURE WORK

7.1 SUMMARY

This dissertation presents the optical properties of nitride semiconductors for visible light emitting applications investigated by cathodoluminescence (CL), which include the simple GaN epitaxial layer and more complicated heterostructures used in light emitting diodes (LED). Characteristic emission peaks associated with different recombination mechanism are identified for wurtzite and cubic GaN, which contribute to knowledge about the band structure near the band edge. The variation of emission energy and intensity with respect to temperature and strain are discussed in both theoretical and experimental aspects. For heterostructures with InGaN/GaN quantum wells, carrier recombination dynamics are studied, and the effect of radiative and non-radiative recombinations on luminescence efficiency are discussed.

Chapter 1 introduces the physical background on light emission in semiconductors. It starts with the fundamental device designs for LEDs (*p*-*n* junction and double heterostructures), and followed by requirements for material systems chosen for light emitting applications. The competences and advantages of nitride semiconductors as successful choices are demonstrated. In order to better understand the optical properties of nitride semiconductors, the theory of radiative recombination is introduced in terms of both semiclassical model and quantum mechanics. The effects of temperature and electric field on emission features are also discussed.

Chapter 2 introduces the experimental technique - cathodoluminescence and time-resolved technique used in the dissertation. The basic information we can get from the cathodoluminescence is the luminescence intensity vs the wavelength, i.e., a spectrum. The time-resolved technique can provide information on recombination lifetimes. The basic principles, experimental setup and work modes of cathodoluminescence are reviewed in this chapter. And examples of their applications on nitride semiconductors are presented as well.

Chapter 3 presents the study on the effect of dislocation density and residual strain on the light emission characteristics of GaN epilayers grown on sapphire. A linear relationship is demonstrated between the exciton emission energy and the in-plane compressive strain calculated with respect to the epilayer which has highest dislocation density. It shows that the exciton emission energy increases with the magnitude of the in-plane compressive strain.

In chapter 4, the fundamental optical transitions in cubic GaN are reported. Excitonic transition, donor-acceptor pair recombination and its phonon replica are well resolved. The temperature dependences of emission energies and intensities are also studied. The donor bound excitons at sufficient low temperatures dissociate into free excitons with increasing temperature. The donor-acceptor pairs recombination turns into the transition between the conduction band and the acceptor states. The experimental results show that the ionization energies for both acceptors and donors are smaller than their counterparts in wurtzite structure, which can contribute to effective doping.

Chapter 5 presents the structural and optical properties of blue, green, and yellow-emitting InGaN/GaN quantum wells (QWs). TEM results show that compositional inhomogeneties in the well get more significant with increasing emission wavelength. Carrier localization associated with these inhomogeneties in the QWs emitting in the blue and green spectral regions is evidenced by a blueshift in the emission energy with temperature, and a constant radiative lifetime under 50 K for the green-emitting QWs. We also observe the absence of strong localization effects and a relatively high internal quantum efficiency of ~ 12 % for the yellow emitting QWs. On the other hand, the effect of non-radiative recombination on luminescence efficiency also varies with the emission wavelength. The fast increase of the non-radiative recombination rate with temperature in the green emitting QWs contributes to the lower efficiency compared with the blue emitting QWs. The possible saturation of non-radiative

recombination above 100 K may explain the unexpected high emission efficiency for the yellow emitting QWs.

Chapter 6 discusses the effects of InGaN underlayers on the electronic and optical properties of visible InGaN/GaN quantum well structures. The introduction of the $In_{0.03}Ga_{0.97}N$ underlayer results in a significant improvement of the QW emission efficiency. And we also observe a blue shift in the emission energy, a reduced recombination lifetime, an increased spatial homogeneity in the QW luminescence, and a weaker internal field across the QWs. These are explained by partial strain relaxation evidenced by reciprocal space mapping of the X-ray diffraction intensity. Moreover, electrostatic potential profiles obtained by electron holography provide evidence for enhanced carrier injection by tunneling from the underlayer into the first QW.

7.2 FUTURE WORK

In this dissertation, spectroscopic method has been applied to study the optical properties of semiconductors and heterostructures, including fundamental band gap, band-edge emission, radiative and non-radiative recombination lifetime, which are critical for achieving high efficient light emitting devices. The recombination through defect states (Shockley-Read-Hall recombination model) and Auger recombination in the spontaneous emission process significantly limit the luminescence efficiency of LEDs. However, the semiconductor laser is very promising to reach a higher efficiency than LED since the light is emitted by the stimulated emission above the threshold condition. This interesting application and important research topic for nitride semiconductors using stimulated emission for laser diodes (LD) has been demonstrated earlier. “The Laser Dream Theater”, which offers high-quality images by projecting light from red, green, and blue lasers onto 50 m wide and 10 m high screen, was demonstrated by Sony at the 2005 World Exposition in Aichi, Japan.

In the stimulated emission process, once one carrier is injected into the active region, it will interact with the external photon and produce an additional photon, which has the same frequency, direction of propagation, and phase as the stimulating photon. And the emission efficiency is mainly determined by carrier injection. To achive a high efficiency laser, the main chanllenge is to reduce the absorption and increase the material gain.

Spectroscopic method is powerful for investigating the laser gain and loss characterisitics. For example, by pumping the cavities with different stripe lengths, the gain and emission spectra can be determined for transverse electric and transverse magnetic polarizations.[1] The optical gain spectrum can also be obtained by measuring the amplified spotaneous emission spectrum near the lasing threshold.[2] Another example is to measure the attenuated photoluminesence light confined in the waveguide in order to determine the loss spectrum.[3] This approach relies on excition-position dependent and polarization-resolved photoluminescence spectra to determine the loss mechanism of the waveguide. This method is in principle transferrable to our CL setup, and the microstructure features can be correlated to the spatial distribution of optical loss, which will shed light on the loss mechanism. It should be noticed that this loss measurement is particularly precise for InGaN material since it has a large Stokes shift [4], which prevents the re-absorption noise in the measurement.

Another intriguing work is to develop CL system with high carrier injection level, which makes the lasing possible without any further elaborated device processing.[5] Typically GaN-based laser requires carrier injection above $10^{19}/cm^2$ to achieve lasing. Once the electron dose of CL can reach that level, the transform from the spontaneous emission to the stimulated emission can be studied. The blue-shift with increasing injection level will be firstly affected by quantum-confined Stark effect and band filling, then by the gain characteristics. Simultaneously, the CL image on the laser facet can be used to analyze the near-field and optical confinement of laser waveguides.

REFERENCES

1. P. Blood, G. M. Lewis, P. M. Smowton, H. Summers, J. Thomson, and J. Lutti, IEEE J. Sel. Topics Quantum Electron. **9**, 1275 (2003).

2. B. W. Hakki and T. L. Paoli, J. Appl. Phys.**46**, 1299 (1975).

3. D. S. Sizov, R. Bhat, A. Heberle, K. Song, and C. Zah, Appl. Phys. Express, **3**, 122104 (2010).

4. F. A. Ponce, S. Srinivasan, A. Bell, L. Geng, R. Liu, M. Stevens, J. Cai, H. Omiya, H. Marui, and T. Tanaka, Phys. Stat. Sol. B **240**, 273 (2003).

5. C. TragerCowan, D. M. Bagnall, F. McGow, W. McCallum, K. P. ODonnell, P. C. Smith, P. J. Wright, B. Cockayne, K. A. Prior, J. T. Mullins, G. Horsburgh, and B. C. Cavenett, J. Cryst. Growth, **159**, 618 (1996).

REFERENCES

CHAPTER 1

1. I. Vurgaftman and J. R. Meyer, J. Appl. Phys. **94**, 3675 (2003).
2. M. P. Maruska and J. J. Tietjen, Appl. Phys. Lett. **15**, 327 (1969).
3. M. Ilegems and H. C. Montgomery, J. Phys. Chem. Solids. **34**, 885 (1973).
4. H. Amano, N. Sawaki, I. Akasaki, and Y. Toyoda, Appl. Phys. Lett. **48**, 353 (1986).
5. S. Nakamura, Jpn. J. Appl. Phys. **30**, L1705 (1991).
6. H. Amano, M. Kito, K. Hiramatsu, and I. Akasaki, Jpn. J. Appl. Phys. **28**, L2112 (1989).
7. S. Nakamura, M. Senoh, and T. Mukai, Jpn. J. Appl. Phys. **30**, L1708 (1991).
8. S. L. Chuang, "Physics of Optoelectronic Devices", (Wiley, New York, 1995), pp 337-344.
9. Y. P. Varshni, Physica **34**, 149-54 (1967).
10. S. Chichibu, T. Azuhata, T. Sota, and S. Nakamura, J. Appl. Phys. **79**, 2784-6 (1996).
11. Y.-H. Cho, G. H. Gainer, A. J. Fischer, J. J. Song, S. Keller, U. K. Mishra, and S. P. DenBaars, Appl. Phys. Lett. **73**, 1370 (1998).
12. H. P. D. Schenk, M. Leroux, and P. de Mierry, J. Appl. Phys. **88**, 1525 (2000).
13. J. Li, K. B. Nam, J. Y. Lin, and H. X. Jiang, Appl. Phys. Lett. **79**, 3245 (2001).
14. A. Bell, S. Srinivasan, C. Plumlee, H. Omiya, F. A. Ponce, J. Christen, S. Tanaka, A. Fujioka, and Y. Nakagawa, J. Appl. Phys. **95**, 4670-4 (2004).
15. P. G. Eliseev, P. Perlin, J. Lee, and M. Osinski, Appl. Phys. Lett. **71**, 569-71 (1997).
16. J. F. Nye, "Physical Properties of Crystals: Their Representation by Tensors and Matrices", (Oxford, Clarendon Press, London, 1985), pp 124-141.
17. T. Takeuchi, S. Sota, M. Katsuragawa, M. Komori, H. Takeuchi, H. Amano, and I. Akasaki, Jpn. J. Appl. Phys. **36**, L382 (1997).
18. J. S. Im, H. Kolmer, J. Off, A. Sohmer, F. Scholz, and A. Hangleiter, Phys. Rev. B **55**, R9435 (1998).
19. C. Wetzel, T. Takeuchi, H. Amano, and I. Akasaki, Phys. Rev. B **62**, R13302 (2000).
20. S. J. Rosner, E. C. Carr, M. J. Ludowise, G. Girolami, and H. I. Erikson, Appl. Phys. Lett. **70**, 420 (1997).
21. T. Koida, S. F. Chichibu, A. Uedono, A. Tsukazaki, M. Kawasaki, T. Sota, Y. Segawa, and H.

Koinuma, Appl. Phys. Lett. **82**, 532 (2003).

CHAPTER 2

22. T. E. Everhart and P. H. Hoff, J. Appl. Phys. **42**, 5837 (1971).

23. K. Kanaya and S. Okayama, J. Phys. D **5**, 43 (1972).

24. B. Wang, D. Bliss, M. Suscavage, S. Swider, R. Lancto, C. Lynch, D. Weyburne, T. Li, and F. A. Ponce, J. Cryst. Growth, **318**, 1030 (2011).

25. T. Ogino, and M. Aoki, Jpn. J. Appl. Phys. **19**, 2395 (1980).

26. J. Neugebauer and C. G. VandeWalle, Appl. Phys. Lett. **69**, 503 (1996).

27. Z. H. Wu, Y. Q. Sun, J. Yin, Y.-Y Fang, J. N. Dai, C. Q. Chen, Q. Y. Wei, T. Li, K. W. Sun, A. M. Fischer, and F. A. Ponce, J. Vac. Sci. Technol. B **29**, 021005 (2011).

28. W. Becker, "Advanced Time-Correlated Single Photon Counting Techniques", (Springer, Berlin, 2005).

CHAPTER 3

29. H. Amano, N. Sawaki, I. Akasaki, and Y. Toyoda, Appl. Phys. Lett. **48**, 353 (1986).

30. S. Nakamura, Jpn. J. Appl. Phys. **30**, L1705 (1991).

31. S. D. Lester, F. A. Ponce, M. G. Craford, and D. A. Steigerwald, Appl. Phys. Lett. **66**, 1249 (1995).

32. M. Leszczynski, T. Suski, H. Teisseyre, P. Perlin, I. Grzegory, J. Jun, S. Porowski, and T. D. Moustakas, J. Appl. Phys. **76**, 4909 (1994).

33. R. R. Reeber, and K. Wang, J. Materials Research, **15**, 40 (1999).

34. J.-M. Wagner and F. Bechstedt, Phys. Rev. B **66**, 115202 (2002).

35. M. Toth, K. Fleischer, and M. R. Phillips, Phys. Rev. B **59**, 1575 (1999).

36. M. A. Reshchikov, F. Shahedipour, R. Y. Korotkov, M. P. Ulmer, and B. W. Wessles, Physica B **105**, 273 (1999).

37. R. Dingle, D. D. Sell, S. E. Stokowski, and M. Ilegems, Phys. Rev. B **4**, 1211 (1971).

38. B. Monemar, Phys. Rev. B **10**, 676 (1974).

39. W. Shan, T. J. Schmidt, X. H. Yang, S. J. Hwang, and J. J. Song, Appl. Phys. Lett. **66**, 985 (1995).

40. B. Gil, O. Briot, and R.-L. Aulombard, Phys. Rev. B **52**, R 17028 (1995).

41. D. Volm, K. Oettinger, T. Streibl, D. Kovalev, M. Ben-Chorin, J. Diener, B. K. Meyer, J. Majewski, L. Eckey, A. Hoffmann, H. Amano, I. Akasaki, K. Hiramatsu, and T. Detchprohm, Phys. Rev. B **53**, 16543 (1996).

42. M. Tchounkeu, O. Briot, B. Gil, J. P. Alexis, and R.-L. Aulombard, J. Appl. Phys. **80**, 5352 (1996).

CHAPTER 4

43. R. Dingle, D. D. Sell, S. E. Stokowski, and M. Ilegems, Phys. Rev. B **4**, 1211(1971).

44. B. Monemar, Phys. Rev. B **10**, 676 (1974).

45. W. Shan, T. J. Schmidt, X. H. Yang, S. J. Hwang, and J. J. Song, Appl. Phys. Lett. **66**, 985 (1995).

46. B. Gil, O. Briot, and R.-L. Aulombard, Phys. Rev. B **52**, R 17028 (1995).

47. C. Merz, M. Kunzer, U. Kaufmann, I. Akasaki, and H. Amano, Semicond. Sci. Technol. **11**, 712 (1996).

48. S. Strite, J. Ruan, Z. Li, A. Salvador, H. Chen, D. J. Smith, W. J. Choyke, and H. Morkoc, J. Vac. Sci. Technol. B **9**, 1924 (1991).

49. S. Miyoshi, K. Onabe, N. Ohkouchi, H. Yaguchi, R. Ito, S. Fukatsu, and Y.Shiraki, J. Cryst. Grow. **124**, 439 (1992).

50. D. Schikora, M. Hankeln, D. J. As, K. Lischka, T. Litz, A. Wagg, T. Buhrowand F. Henneberger, Phys. Rev. B **54**, R8381 (1996).

51. H. Okumura, K. Ohta, G. Feuillet, K. Balakrishnan, S. Chichibu, H. Hamaguchi, P. Hacke, and S. Yoshida, J. Cryst. Grow. **178**, 113 (1997).

52. D. J. As, S. Potthast, J. Schörmann, S. F. Li, K. Lischka, H. Nagasawa, and M. Abe, Materials Science Forum, **527-529**, 1489 (2002).

53. Q. Y. Wei, T. Li, J. Y. Huang, F. A. Ponce, E. Tschumak, A. Zado, and D. J. As, Appl. Phys. Lett. **100**, 142108 (2012).

54. D. J. As, F. Schmilgus, C. Wang, B. Schöttker, D. Schikora, and K. Lischka, Appl. Phys. Lett. **70**, 1311 (1997).

55. G. Ramirez-Flores, H. Navarro-Contreras, A. Lastras-Martinez, R. C. Powell, and J. E. Greene, Phys. Rev. B **50**, 8433 (1994).

56. J. Menniger, U. Jahn, O. Brandt, H. Yang, and K. Ploog, Phys. Rev. B **53**, 1881 (1996).

57. A. Zado, E. Tschumak, K. Lischka, and D. J. As, Semicond. Sci. Technol. **27**, 035020 (2012).

CHAPTER 5

58. F. A. Ponce and D. P. Bour, Nature **386**, 351 (1997).

59. S. Chichibu, T. Azuhata, T. Sota, and S. Nakamura, Appl. Phys. Lett. **69**, 4188 (1996).

60. T. Mukai, M. Yamada, and S. Nakamura, Jpn. J. Appl. Phys. **37**, L1358 (1998).

61. T. Takeuchi, C. Wetzel, S. Yamaguchi, H. Sakai, H. Amano, I. Akasaki, Y. Kaneko, S. Nakagawa, Y. Yamaoka, and N. Yamada, Appl. Phys. Lett. **73**, 1691 (1998).

62. J. Bai, T. Wang, and S. Sakai, J. Appl. Phys. **88**, 4729 (2000).

63. D. Cherns, S. J. Henley, and F. A. Ponce, Appl. Phys. Lett. **78**, 2691 (2001).

64. A. Hangleiter, F. Hitzel, C. Netzel, D. Fuhrmann, U. Rossow, G. Ade, and P. Hinze, Phys. Rev. Lett. **95**, 127402 (2005).

65. S. Chichibu, K. Wada, and S. Nakamura, Appl. Phys. Lett. **71**, 2346 (1997).

66. T. Li, A. M. Fischer, Q. Y. Wei, F. A. Ponce, T. Detchprohm, and C. Wetzel, Appl. Phys. Lett. **96**, 031906 (2010).

67. Y.-H. Cho, G. H. Gainer, A. J. Fischer, J. J. Song, S. Keller, U. K. Mishra, and S. P. DenBaars, Appl. Phys. Lett. **73**, 1370 (1998).

68. H. P. D. Schenk, M. Leroux, and P. de Mierry, J. Appl. Phys. **88**, 1525 (2000).

69. J. Li, K. B. Nam, J. Y. Lin, and H. X. Jiang, Appl. Phys. Lett. **79**, 3245 (2001).

70. A. Bell, S. Srinivasan, C. Plumlee, H. Omiya, F. A. Ponce, J. Christen, S. Tanaka, A. Fujioka, and Y. Nakagawa, J. Appl. Phys. Lett. **95**, 4670 (2004).

71. Y. Narukawa, S. Saijou, Y. Kawakami, Sg. Fujita, T. Mukai, and S. Nakamura, Appl. Phys. Lett. **74**, 558 (1999).

72. R. C. Miller, D. A. Kleinman, W. A. Nordland, Jr., and A. C. Gossard, Phys. Rev. B **22**, 863 (1980).

73. Y. Narukawa, Y. Kawakami, Sg. Fujita, and S. Nakamura, Phys. Rev. B **59**, 10823 (1998).

74. Y. Kawakami, K. Omae, A. Kaneta, K. Okamoto, Y. Narukawa, T. Mukai, and Sg. Fujita, J. Phys.: Condens. Matter **13**, 6993 (2001).

75. C. Wetzel, T. Salagaj, T. Detchprohm, P. Li, and J. S. Nelson, Appl. Phys. Lett. **85**, 866 (2004).

CHAPTER 6

76. F. A. Ponce, S. Srinivasan, A. Bell, L. Geng, R. Liu, M. Stevens, J. Cai, H. Omiya, H. Marui, and S. Tanaka, Phys. Stat. Sol. B **240**, 273 (2003).

77. S. Chichibu, T. Azuhata, T. Sota, and S. Nakamura, Appl. Phys. Lett. **69,** 4188 (1996).

78. S. Srinivasan, F. Bertram, A. Bell, F. A. Ponce, S. Tanaka, H. Omiya, and Y. Nakagawa, Appl. Phys. Lett. **80**, 550 (2002).

79. S. D. Lester, F. A. Ponce, M. G. Craford, and D. A. Steigerwald, Appl. Phys. Lett. **66**, 1249 (1995).

80. T. Takeuchi, C. Wetzel, S. Yamaguchi, H. Sakai, H. Amano, I. Akasaki, Y. Kaneko, S. Nakagawa, Y. Yamaoka, and N. Yamada, Appl. Phys. Lett. **73**, 1691 (1998).

81. T. Akasaka, H. Gotoh, T. Saito, and T. Makimoto, Appl. Phys. Lett. **85**, 3089 (2004).

82. J. K. Son, S. N. Lee, T. Sakong, H. S. Paek, O. Nam, Y. Park, J. S. Hwang, J. Y. Kim, and Y. H. Cho, J. Cryst. Growth **287**, 558 (2006).

83. K. M. Kelchner, Y. D. Lin, M. T. Hardy, C. Y. Huang, P. S. Hsu, R. M. Farrell, D. A. Haeger, H. C. Kuo, F. Wu, K. Fujito, D. A. Cohen, A. Chakraborty, H. Ohta, J. S. Speck, S. Nakamura, and S. P. DenBaars, Appl. Phys. Express **2**, 071003 (2009).

84. J. P. Liu, Y. Zhang, Z. Lochner, S.-S. Kim, H. Kim, J.-H. Ryou, S.-C. Shen, P. D. Yoder, R. D. Dupuis, Q. Y. Wei, K. W. Sun, A. M. Fischer, and F. A. Ponce, J. Cryst. Growth **315**, 272 (2011).

85. A. J. Pidduck, D. J. Robbins, A. G. Cullis, W. Y. Leong, and A. M. Pitt, Thin Solid Films **222**, 78 (1992).

86. J. Cai and F. A. Ponce, J. Appl. Phys. **91**, 9856 (2002).

87. F. A. Ponce, Ann. Phys. (Berlin) **523**, 75 (2011).

CHAPTER 7

88. P. Blood, G. M. Lewis, P. M. Smowton, H. Summers, J. Thomson, and J. Lutti, IEEE J. Sel. Topics Quantum Electron. **9**, 1275 (2003).

89. B. W. Hakki and T. L. Paoli, J. Appl. Phys.**46**, 1299 (1975).

90. D. S. Sizov, R. Bhat, A. Heberle, K. Song, and C. Zah, Appl. Phys. Express, **3**, 122104 (2010).

91. F. A. Ponce, S. Srinivasan, A. Bell, L. Geng, R. Liu, M. Stevens, J. Cai, H.Omiya, H. Marui, and T. Tanaka, Phys. Stat. Sol. B **240**, 273 (2003).

92. C. TragerCowan, D. M. Bagnall, F. McGow, W. McCallum, K. P. ODonnell, P. C. Smith, P. J. Wright, B. Cockayne, K. A. Prior, J. T. Mullins, G. Horsburgh, and B. C. Cavenett, J. Cryst. Growth, **159**, 618 (1996).

APPENDIX

LIST OF PUBLICATIONS DURING THE STUDY TOWARDS THE DOCTORAL DEGREE

Publications that resulted from my work at ASU are listed below:

[1] Q. Y. Wei, T. Li, J. Y. Huang, F. A. Ponce, E. Tschumak, A. Zado, and D. J. As, "Free carrier accumulation at cubic AlGaN/GaN heteojunctions", Appl. Phys. Lett. 100, 142108 (2012).

[2] Q. Y. Wei, T. Li, Y. Huang, J. Y. Huang, Z. T. Chen, T. Egawa, and F. A. Ponce, "Compositional instability in InAlN/GaN lattice-matched epitaxy", Appl. Phys. Lett. 100, 092101 (2012).

[3] B. Wang, D. Bliss, M. Suscavage, S. Swider, R. Lancto, C. Lynch, D. Weyburne, T. Li, and F. A. Ponce, "Ammonothermal growth of high quality GaN crystals on HVPE template seeds", J. Cryst. Growth, 318 (2011) 1030.

[4] Z. H. Wu, Y. Q. Sun, J. Yin, Y. Y. Fang, J. N. Dai, C. Q. Chen, Q. Y. Wei, T. Li, K. W. Sun, A. M. Fischer, and F. A. Ponce, "Reduction of structural defects in a-plane GaN epitaxy by use of periodic hemispherical patterns in r-plane sapphire substrates ", J. Vac. Sci. Technol. B 29, 021005 (2011).

[5] Y. Q. Sun, Z. H. Wu, J. Yin, Y. Y. Fang, H. Wang, C. H. Yu, X. Hui, C. Q. Chen, Q. Y. Wei, T. Li, K. W. Sun, and F. A. Ponce, " High quality a-plane GaN films grown on cone-shaped patterned r-plane sapphire substrates ", Thin. Solid. Films. 519, 2508 (2011).

[6] T. Li, A. M. Fischer, Q. Y. Wei, F. A. Ponce, T. Detchprohm, and C. Wetzel, " Carrier localization and nonradiative recombination in yellow emitting InGaN quantum wells ", Appl. Phys. Lett. 96, 031906 (2010).

[7] Q. Y. Wei, T. Li, Z. H. Wu, and F. A. Ponce, "In-plane polarization of GaN-based heterostructures with arbitrary crystal orientation", Phys. Stat. Sol. A 207, 2226 (2010).

[8] R. Li, J. M. Zhang, L. Chen, H. Zhao, Z. Yang, T. Yu, D. Li, Z. C. Liu, W. H. Chen, Z. J. Yang, G. Y. Zhang, Z. Z. Gan, X. D. Hu, Q. Y. Wei, T. Li, and F.A. Ponce, "Donor-related cathodoluminescence of p-AlGaN electron blocking layer embedded in ultraviolet laser diode structure", Appl. Phys. Lett. 94, 211103 (2009).